Euro. Jnl of Applied Mathematics (2010), *vol.* 21, *pp.* 519–556.
doi:10.1017/S0956792510000203

Finite-element approximation of coupled surface and grain boundary motion with applications to thermal grooving and sintering

JOHN W. BARRETT[1], HARALD GARCKE[2] and ROBERT NÜRNBERG[1]

[1]*Department of Mathematics, Imperial College London, London SW7 2AZ, UK*
email: {j.barrett,robert.nurnberg}@imperial.ac.uk

[2]*NWF I – Mathematik, Universität Regensburg, 93040 Regensburg, Germany*
email: harald.garcke@mathematik.uni-regensburg.de

(*Received 26 May 2009; revised 10 June 2010; accepted 13 June 2010; first published online 21 July 2010*)

We study the coupled surface and grain boundary motion in bi- and tricrystals in three-space dimensions, building on previous work by the authors on the simplified two-dimensional case. The motion of the interfaces, which in this paper are presented by two-dimensional hypersurfaces, is described by two types of normal velocities: motion by mean curvature and motion by surface diffusion. Three hypersurfaces meet at triple-junction lines, where junction conditions need to hold. Similarly, boundary conditions are prescribed where an interface meets an external boundary, and these conditions naturally give rise to contact angles. We present a variational formulation of the flows, which leads to a fully practical finite-element approximation that exhibits excellent mesh properties, with no mesh smoothing or remeshing required in practice. For the introduced parametric finite-element approximation we show well posedness and, in general, unconditional stability, i.e. there is no restriction on the chosen time-step size. Moreover, the induced discrete equations are linear and easy to solve. A generalisation to anisotropic surface energies is straightforward. Several numerical results in two- and three-space dimensions are presented, including simulations for thermal grooving and sintering. Three-dimensional simulations featuring quadruple junction points, non-standard boundary contact angles and fully anisotropic surface energies are also presented.

1 Introduction

In many applications the dynamics of interfaces in polycrystalline microstructures is given by a coupling of surface diffusion to grain boundary motion. It is well known that a grain boundary, which is attached to an exterior surface, leads to a groove at the triple-junction line, where the grain boundary meets the two exterior boundaries of a bicrystal. The establishing and deepening of the groove is a direct result of the local minimisation of the combined surface energies of the exterior surface and the grain boundary, and this process is often referred to as thermal grooving. The grain boundary will migrate according to mean curvature flow, while the evolution of the two exterior boundaries is given by surface diffusion. Mean curvature flow is a second-order parabolic equation and surface diffusion is a fourth-order geometric evolution equation. These two evolution laws

are coupled at the triple line via boundary conditions stating force and mass balance laws and a continuity condition for chemical potentials.

The mean curvature flow is the steepest descent dynamics of the area functional with respect to the L^2 inner product. If we decrease area with respect to the H^{-1} inner product, we obtain motion by surface diffusion (see [46] for details). If these flows are coupled at boundaries of surfaces one obtains an evolution law which decreases the total surface area (see Proposition 2.1).

The evolution of surface grooves at grain boundaries was first studied by Mullins ([37]) and this has led to many further studies in materials science, physics and applied mathematics (see e.g. [14, 31, 32, 40, 42, 47] and the references therein). In particular, the question arose whether the appearance of the surface groove will slow down the velocity of the grain boundary. In this context travelling wave solutions have been studied in the literature (see [31, 37]). But recent studies seem to indicate that the grain groove only has a minimal effect on the grain boundary motion. However, it seems to be the case that the anisotropy of the exterior surface can have a strong influence on the dynamics of the grain boundary. For more background on the effect of the thermal groove on the velocity of the grain boundary we refer to the discussion in [34], and the references therein.

The coupling of grain boundary motion to free surface flow given by surface diffusion also plays an important role in sintering processes such as the sintering of powder components or the sintering of ice (see e.g. the reviews [10, 39]). Similar to the case of grain boundary motion, the main driving force here is the reduction of surface energy.

So far numerical studies for coupled mean curvature flow and surface diffusion have been restricted to the planar case, or to very simplified geometries in three dimensions. Mathematical approaches for the two-dimensional case include finite-element and finite-difference approximations for parametric formulations (see e.g. [2, 14–16, 33, 35, 40–42, 44, 45]), numerical approximations of graph formulations (see e.g. [48, 50, 51]), as well as finite-difference and finite-element methods for phase field models (see e.g. [3, 36]). Here it should be noted that in the latter paper the authors studied a phase field model, which in the asymptotic limit does not recover surface diffusion for the material surface, but a motion law that combines surface diffusion and surface attachment limited kinetics (see [3, Equation (1.3)]). The interested reader is referred to [5] for further details. Numerical studies for coupled mean curvature flow and surface diffusion in three-space dimensions are so far restricted to very simplified geometries (see e.g. [34, 49, 52]). Let us mention here that in [34] a radially symmetric grain is studied and that the authors in [49] compute for a simplified model, where the fourth-order flow by surface diffusion is replaced by the second-order conserved mean curvature flow. The latter authors use the software package Surface Evolver, [11], for a discrete gradient descent method that is intended to mimic the physical gradient flow.

In this paper, based on our earlier work for the planar case in [2], we develop for the first time a numerical approach for coupled surface diffusion and grain boundary motion for truly three-dimensional geometries. In particular, we are able to handle the following situations:

- Fully anisotropic surface energies and mobilities.
- Contacts with a fixed outer boundary that lead to non-90° angle conditions.

https://doi.org/10.1017/S0956792510000203 Published online by Cambridge University Press

- Tricrystalline geometries with four triple lines meeting at a quadruple junction point.

We will present, among others, numerical results for the following phenomena:

- Relaxation of a grain attached to an external surface towards a radially symmetric profile (see Figure 13). The attained radially symmetric profile is related to the radially symmetric computations in [34].
- Relaxation of a truly three-dimensional moving grain boundary towards a two-dimensional 'flat' travelling wave profile (see Figure 17). On the basis of our numerical studies we conjecture that the two-dimensional travelling wave profile studied in [31,37] is stable also with respect to truly three-dimensional perturbations.
- Sintering of several particles including examples where small particles grow at the expense of larger ones (see Figure 20).
- Singularity formation in cases where a free surface meets a polyhedral boundary with a non-90° contact angle (see Figure 12). Similar phenomena are well known in the theory of capillary surfaces (see e.g. [17, Chapter 6] or [30]).
- The effect of anisotropy on the groove profile (see Figure 8), and on the sintering of particles (see Figure 24).

The outline of the paper is as follows. In Section 2 we derive the governing equations in a variational context, show energy bounds and derive a weak formulation. A new finite-element approximation based on the variational approach in Section 2 is derived in Section 3, where we also show existence, uniqueness and stability results for the proposed scheme. In Section 4 we discuss briefly how to solve the resulting discrete systems in practice. Finally, we present numerical results for the above mentioned phenomena in Section 5 (for two-space dimensions) and Section 6 (for three-space dimensions).

2 Variational formulation and an energy law

In this section we derive the geometric evolution equations for a cluster of surfaces in detail, where the cluster is used to model the coupled surface and grain boundary motion in a bicrystal. Hence we assume that the surface cluster is connected and consists of three hypersurfaces with boundaries, which all meet at a single triple-junction line. In addition, all or some of the hypersurfaces may intersect an external boundary. Two possible such type of set-ups can be seen in Figures 10 and 17. Generalisations to more complicated set-ups, including to clusters with quadruple junction points, where four triple-junction lines meet, are straightforward (see [8]). But for the sake of clarity and brevity we restrict ourselves to the simpler situation described above in the majority of this paper. In order to parameterise the surfaces we choose a collection of domains $\Omega_i \subset \mathbb{R}^2$, $i = 1 \to 3$. The surface cluster is then given with the help of parameterisations $\vec{x}_i : \Omega_i \times [0,T] \to \mathbb{R}^3$ with $\vec{x}_i(\Omega_i, t) = \Gamma_i(t)$, $i = 1 \to 3$, being the surfaces making up the cluster. Here and throughout we will often use the shorthand notation $\vec{x}(\Omega, t) = \Gamma(t)$, where $\Omega := (\Omega_1, \Omega_2, \Omega_3)$ and $\Gamma(t) := (\Gamma_1(t), \Gamma_2(t), \Gamma_3(t))$. Relevant reference domains in this paper are the unit disk in $\mathbb{R}^2$; $\Omega_i = \mathbb{B}_1^2$, where $\mathbb{B}_r^d := \{\vec{z} \in \mathbb{R}^d : |\vec{z}| < r\}$, with boundary $\partial\Omega_i = \mathbb{S}^1$, i.e. the unit circle in $\mathbb{R}^2$, as well as the open annulus $\Omega_i = \mathbb{B}_2^2 \setminus \overline{\mathbb{B}_1^2}$.

https://doi.org/10.1017/S0956792510000203 Published online by Cambridge University Press

Fundamental for the following considerations will be the identities

$$\Delta_s \vec{x}_i = \vec{\varkappa}_i \equiv \varkappa_i \vec{\nu}_i, \quad i = 1 \to 3, \tag{2.1}$$

which for a single surface, with or without boundary, was first used by Dziuk ([21]) to design a finite-element method for geometric partial differential equations and mean curvature flow (see also [22]). The identity (2.1) is well known from surface geometry (see e.g. [19]), where ∇_s is the surface (tangential) gradient, $\Delta_s \equiv \nabla_s \cdot \nabla_s$ is the surface Laplacian (Laplace–Beltrami operator), $\vec{x}_i$ is a parameterisation of Γ_i, $\vec{\varkappa}_i$ is the mean curvature vector, $\varkappa_i$ is the sum of the principal curvatures and $\vec{\nu}_i$ is a unit normal to Γ_i. Here we use the sign convention that $\varkappa_i$ is positive, if the surface Γ_i is curved in the direction of the normal $\vec{\nu}_i$; e.g. a sphere with outer normal has negative mean curvature. Of general interest are the motions of the surface cluster by mean curvature flow

$$\mathscr{V}_i = \varkappa_i, \quad i = 1 \to 3, \tag{2.2}$$

where $\mathscr{V}_i := [\vec{x}_i]_t \cdot \vec{\nu}_i$ is the normal velocity of the surface Γ_i; and the motion by surface diffusion

$$\mathscr{V}_i = -\Delta_s \varkappa_i, \quad i = 1 \to 3. \tag{2.3}$$

These flows, for general surface clusters with an arbitrary number of triple-junction lines and quadruple junction points, were investigated in [8]. However, in this paper we want to restrict our attention to the following motion, which has physical applications in thermal grooving and sintering; recall Section 1. In particular, the surfaces Γ_1 and Γ_2 will model a material surface, while the surface Γ_3 models a grain boundary that separates two grains within the material. Hence the three surfaces of the cluster evolve by

$$\mathscr{V}_i = -\Delta_s \varkappa_i, \ i = 1 \to 2 \quad \text{and} \quad \mathscr{V}_3 = \varkappa_3, \tag{2.4}$$

i.e. the two material surfaces move by surface diffusion and the third surface, modelling the grain boundary, undergoes motion by mean curvature. Here, for simplicity, we have set all the physicial constants, such as the diffusion constants in the surface diffusion equations, to unity. In addition to the differential equations in (2.4), certain boundary conditions have to be prescribed at the boundaries of the surfaces Γ_i, $i = 1 \to 3$, and this will be outlined in the following part of this paper.

In order to describe the necessary conditions that need to hold at the triple-junction line, where the three surfaces meet, as well as on the boundary intersection lines, where a single surface meets the external boundary, we introduce the following notation. Assume that $\partial\Omega_i$, the boundary of Ω_i, is partitioned into $\partial_j\Omega_i$, $j = 1 \to I_P^i$, $I_P^i \geqslant 1$. Then the triple-junction line $\mathscr{T}$ is parameterised with the help of the partitioned boundaries $\partial_j\Omega_i$, $j = 1 \to I_P^i$, $i = 1 \to 3$. In particular, we assume that there exists a triplet (p_1, p_2, p_3) such that

$$\mathscr{T}(t) := \vec{x}_1(\partial_{p_1}\Omega_1, t) = \vec{x}_2(\partial_{p_2}\Omega_2, t) = \vec{x}_3(\partial_{p_3}\Omega_3, t). \tag{2.5a}$$

The conditions that need to hold at a triple-junction line (see e.g. [12, 27]) can then be

https://doi.org/10.1017/S0956792510000203 Published online by Cambridge University Press

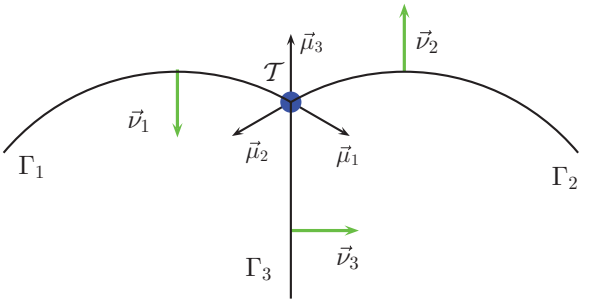

FIGURE 1. (Colour online) Sketch of the local orientation of $(\Gamma_1, \Gamma_2, \Gamma_3)$ at the triple-junction line $\mathscr{T}$ (**blue**). Depicted above is a plane that is perpendicular to $\mathscr{T}$.

formulated as follows. In addition to the attachment conditions (2.5*a*), we require that

$$\vec{\mu}_1 + \vec{\mu}_2 + \vec{\mu}_3 = \vec{0} \quad \text{on } \mathscr{T}, \tag{2.5b}$$

where $\vec{\mu}_i$ denotes the conormal, i.e. the intrinsic outer unit normal to $\partial\Gamma_i$, the boundary of Γ_i, which lies within the tangent plane of Γ_i. The identity (2.5*b*) is a force balance condition on the triple-junction line $\mathscr{T} \subset \mathbb{R}^3$. In the case of equal isotropic energies, as considered here, the condition (2.5*b*) leads to the well-known 120° angle condition at the triple-junction line. As the surface diffusion flow equations in (2.4) are of fourth order, we require additional boundary conditions. To formulate these conditions we need to choose an appropriate orientation of the three surface normals. Hence from now on we assume that the normals are chosen such that $(\vec{\nu}_i, \vec{\mu}_i)$, $i = 1 \to 3$, all have the same orientation in an arbitrary plane orthogonal to $\mathscr{T}$ (see Figure 1). Note that we really only need this to hold for $i = 1 \to 2$, but the stated condition represents no loss of generality. Then the additional boundary conditions are

$$\vec{\mu}_1 \,.\, \nabla_s \varkappa_1 = \vec{\mu}_2 \,.\, \nabla_s \varkappa_2 \quad \text{on } \mathscr{T}, \tag{2.5c}$$

$$\varkappa_1 + \varkappa_2 = 0 \quad \text{on } \mathscr{T}, \tag{2.5d}$$

where (2.5*c*) is a flux balance condition and (2.5*d*) is a chemical potential continuity condition that need to hold on the triple-junction line.

Since the diffusion constants were set to unity, the material fluxes along the material surfaces are given by $-\nabla_s \varkappa_1$ and $\nabla_s \varkappa_2$ (see e.g. [18]). The different signs are a consequence of our sign convention for the curvature (see Figure 1). Equation (2.5*c*) requires that the diffusive fluxes balance each other at the triple-junction line. The condition (2.5*d*) was derived by Novick–Cohen (see equation (5.18) in [38]) in a sharp interface asymptotics for an Allen–Cahn/Cahn–Hilliard system. In this context we also refer to equation (37) in [27], equations (5) and (8) with $\beta = 0$ in [5] and equation (12) in [42]. The two conditions (2.5*c*,*d*) also guarantee a free energy inequality (see Proposition 2.1), and hence imply that the overall system is thermodynamically consistent.

The boundary lines, where a surface Γ_i meets an external boundary, can be parameterised in a similar fashion to (2.5*a*). In cases where this external boundary is itself a smooth

https://doi.org/10.1017/S0956792510000203 Published online by Cambridge University Press

hypersurface, it is sufficient to consider a single smooth bounded domain $\mathscr{D} \subset \mathbb{R}^3$ with boundary $\partial\mathscr{D}$. However, in practice it is often of interest to consider domains, where the boundary is only piecewise differentiable. In order to be able to model such situations, e.g. when $\mathscr{D}$ is a cube, we assume that $I_D \geqslant 1$ smooth, not necessarily bounded, C^1-domains $\mathscr{D}_j \subset \mathbb{R}^3$, $j = 1 \to I_D$, with boundaries $\partial\mathscr{D}_j$ are given, and that parts of the boundaries of the surfaces Γ_i, $i = 1 \to 3$, are constrained to lie on these external boundaries. In general there will be $I_B \geqslant 0$ such boundary lines, where the case $I_B = 0$ corresponds to no boundary intersections being present. Let the boundary line $\mathscr{B}_k$ be given by the triplet (s_k, p_k, d_k) such that, similarly to (2.5*a*),

$$\mathscr{B}_k(t) := \vec{x}_{s_k}(\partial_{p_k}\Omega_{s_k}, t) \subset \partial\mathscr{D}_{d_k}, \quad k = 1 \to I_B. \tag{2.6}$$

It should be noted that if $I_D > 1$ then (2.6), in general, does not *a priori* guarantee that the boundary lines $\mathscr{B}_k$, $k = 1 \to I_B$, remain attached to the boundary of the 'virtual' domain

$$\mathscr{D} := \bigcap_{j=1}^{I_D} \mathscr{D}_j. \tag{2.7}$$

However, in all the flows that we will consider in practice, this will indeed always be the case. We remark that when $\mathscr{D}$ is the unit cube, then a possible construction via (2.7) is $\mathscr{D}_1 = (0,1) \times \mathbb{R}^2$, $\mathscr{D}_2 = \mathbb{R} \times (0,1) \times \mathbb{R}$ and $\mathscr{D}_3 = \mathbb{R}^2 \times (0,1)$ with $I_D = 3$.

Let $\vec{n}_j$ be the outer unit normal to $\partial\mathscr{D}_j$, $j = 1 \to I_D$. Then (2.6) can be equivalently formulated as $\vec{x}_{s_k}(\partial_{p_k}\Omega_{s_k}) \subset \partial\mathscr{D}_{d_k}$ at time $t = 0$ together with

$$\vec{n}_{d_k} \,.\, \vec{x}_{s_k,t} = 0 \quad \text{on } \mathscr{B}_k, \quad k = 1 \to I_B. \tag{2.8a}$$

Moreover, we require that

$$\vec{n}_{d_k} \,.\, \vec{v}_{s_k} = \varrho_k \quad \text{on } \mathscr{B}_k, \quad k = 1 \to I_B, \tag{2.8b}$$

where $\varrho_k \in \mathbb{R}$, $k = 1 \to I_B$ are given constants. Here, for a fixed k, ϱ_k denotes the change in contact energy density in the direction of $-\vec{v}_{s_k}$ that the two phases separated by the interface Γ_{s_k} have with the external boundary $\partial\mathscr{D}_{d_k}$. In most cases, the contact energies are assumed to be the same, so that $\varrho_k = 0$ and (2.8*b*) is equivalent to a 90° contact angle condition. In general, this need not be the case and different contact energy densities give rise to a non-zero tangential forcing. See (2.18*a*) and Proposition 2.1 for more details in the anisotropic case. For the surfaces Γ_1 and Γ_2, which move by surface diffusion, we require in addition to (2.8*b*) the no-flux boundary conditions

$$\vec{\mu}_{s_k} \,.\, \nabla_s \varkappa_{s_k} = 0 \quad \text{on } \mathscr{B}_k, \quad k \in \{l = 1 \to I_B : s_l \in \{1,2\}\}. \tag{2.8c}$$

For more information on the above conditions we refer to [8].

On adapting the results derived in [8], it is not difficult to show that (2.4) with (2.5*a–d*) and (2.8*a–c*) is a gradient flow of the total surface area

$$E(\Gamma) = |\Gamma| := \sum_{i=1}^{3} \int_{\Gamma_i} 1 \, \mathrm{d}\mathscr{H}^2, \tag{2.9}$$

https://doi.org/10.1017/S0956792510000203 Published online by Cambridge University Press

where $\mathscr{H}^d$ is the d-dimensional Hausdorff measure in $\mathbb{R}^3$, i.e. the total surface area is monotonically decreasing in time.

We now outline the generalisations of the flow (2.4) with (2.5*a–d*) and (2.8*a–c*) to the case of fully anisotropic surface energies. In this case the isotropic free energy (2.9) is replaced by the anisotropic energy

$$E_\gamma(\Gamma) = |\Gamma|_\gamma := \sum_{i=1}^{3} |\Gamma_i|_{\gamma_i} := \sum_{i=1}^{3} \int_{\Gamma_i} \gamma_i(\vec{\nu}_i)\, \mathrm{d}\mathscr{H}^2, \tag{2.10}$$

where $\gamma := (\gamma_1, \gamma_2, \gamma_3)$ with γ_i, $i = 1 \to 3$, being positive and absolutely homogeneous functions of degree one; i.e. in particular $\gamma_i : \mathbb{R}^3 \to \mathbb{R}_{\geqslant 0}$ with $\gamma_i(\vec{p}) > 0$ if $\vec{p} \neq \vec{0}$ and

$$\gamma_i(\lambda\,\vec{p}) = |\lambda|\,\gamma_i(\vec{p}) \quad \forall\ \vec{p} \in \mathbb{R}^3,\ \forall\ \lambda \in \mathbb{R} \quad \Rightarrow \quad \gamma_i'(\vec{p})\,.\,\vec{p} = \gamma_i(\vec{p}) \quad \forall\ \vec{p} \in \mathbb{R}^3 \setminus \{\vec{0}\}, \tag{2.11}$$

where γ_i' is the gradient of γ_i. In the isotropic case we have that

$$\gamma_i(\vec{p}) = \varsigma_i\,|\vec{p}| \quad \text{with} \quad \varsigma_i > 0, \quad i = 1 \to 3, \tag{2.12}$$

which implies that $\gamma_i(\vec{\nu}_i) = \varsigma_i$; and so $|\Gamma_i|_{\gamma_i}$ in (2.10) reduces to $\varsigma_i\,|\Gamma_i|$, the scaled surface area of Γ_i. In the isotropic equal energy density case we have, in addition, that $\varsigma_i = 1$, $i = 1 \to 3$; and so $E_\gamma(\Gamma)$ reduces to $E(\Gamma)$, the surface area of Γ.

In order to define anisotropic mean curvature flow and anisotropic surface diffusion, we introduce the Cahn–Hoffmann vectors (see [13]),

$$\vec{\nu}_{\gamma,i} := \gamma_i'(\vec{\nu}_i), \quad i = 1 \to 3; \tag{2.13a}$$

and define the weighted mean curvatures as

$$\varkappa_{\gamma,i} := -\nabla_s\,.\,\vec{\nu}_{\gamma,i}, \quad i = 1 \to 3. \tag{2.13b}$$

Then the anisotropic generalisation of (2.4) is given by

$$\mathscr{V}_i = -\nabla_s\,.\,(\beta_i(\vec{\nu}_i)\,\nabla_s\,\varkappa_{\gamma,i}),\ i = 1 \to 2 \quad \text{and} \quad \mathscr{V}_3 = \beta_3(\vec{\nu}_3)\,\varkappa_{\gamma,3}, \tag{2.14}$$

where $\beta_i : \mathbb{S}^2 \to \mathbb{R}_{>0}$, $i = 1 \to 3$ are kinetic coefficients, and are assumed to be smooth, even and positive functions defined on the unit sphere $\mathbb{S}^2 \subset \mathbb{R}^3$.

Naturally, the triple-junction line conditions (2.5*a–d*), as well as the boundary intersection conditions (2.8*a–c*), need to be generalised to the anisotropic setting. Of course, the attachment conditions (2.5*a*) still need to hold. In addition, the following conditions have to hold on the triple-junction line:

$$\sum_{i=1}^{3} [\gamma_i(\vec{\nu}_i)\,\vec{\mu}_i - (\gamma_i'(\vec{\nu}_i)\,.\,\vec{\mu}_i)\,\vec{\nu}_i] = \vec{0} \quad \text{on } \mathscr{T}, \tag{2.15a}$$

$$\vec{\mu}_1\,.\,\beta_1(\vec{\nu}_1)\,\nabla_s\,\varkappa_{\gamma,1} = \vec{\mu}_2\,.\,\beta_2(\vec{\nu}_2)\,\nabla_s\,\varkappa_{\gamma,2} \quad \text{on } \mathscr{T}, \tag{2.15b}$$

$$\varkappa_{\gamma,1} + \varkappa_{\gamma,2} = 0 \quad \text{on } \mathscr{T}. \tag{2.15c}$$

We note that in the isotropic case, (2.12), it holds that $\vec{\nu}_{\gamma,i} = \varsigma_i\,\vec{\nu}_i$ with $\varkappa_{\gamma,i} = \varsigma_i\,\varkappa_i$, and

https://doi.org/10.1017/S0956792510000203 Published online by Cambridge University Press

hence (2.15*a–c*) with $\beta = (1,1,1)$, on recalling that $\vec{\nu}_i \,.\, \vec{\mu}_i = 0$, simplify to

$$\text{(a)}\ \ \varsigma_1 \vec{\mu}_1 + \varsigma_2 \vec{\mu}_2 + \varsigma_3 \vec{\mu}_3 = \vec{0},\ \text{(b)}\ \ \varsigma_1 \vec{\mu}_1 \,.\, \nabla_s \varkappa_1 = \varsigma_2 \vec{\mu}_2 \,.\, \nabla_s \varkappa_2,\ \text{(c)}\ \ \varsigma_1 \varkappa_1 + \varsigma_2 \varkappa_2 = 0 \quad (2.16)$$

on $\mathscr{T}$, respectively. Hence we observe that (2.15*a–c*) collapse to (2.5*b–d*) in the isotropic equal energy density case. We remark that the condition (2.16a) is the well-known Young's law, which is equivalent to the angle condition $\frac{\sin\theta_1}{\varsigma_1} = \frac{\sin\theta_2}{\varsigma_2} = \frac{\sin\theta_3}{\varsigma_3}$, where

$$\theta_1 = \sphericalangle(\vec{\mu}_2, \vec{\mu}_3), \quad \theta_2 = \sphericalangle(\vec{\mu}_3, \vec{\mu}_1) \quad \text{and} \quad \theta_3 = \sphericalangle(\vec{\mu}_1, \vec{\mu}_2) \quad \text{on } \mathscr{T} \tag{2.17}$$

are the dihedral angles of the tangent planes at the triple-junction line.

Similarly, the boundary intersection conditions (2.8*b,c*) can be generalised to the anisotropic case as follows. Apart from (2.8*a*), the following need to hold

$$\vec{n}_{d_k} \,.\, \gamma'_{s_k}(\vec{\nu}_{s_k}) = \varrho_k \quad \text{on } \mathscr{B}_k, \quad k = 1 \to I_B, \tag{2.18a}$$

$$\vec{\mu}_{s_k} \,.\, \nabla_s \varkappa_{\gamma,s_k} = 0 \quad \text{on } \mathscr{B}_k, \quad k \in \{l = 1 \to I_B : s_l \in \{1,2\}\}, \tag{2.18b}$$

where, as before, $\varrho_k \in \mathbb{R}$, $k = 1 \to I_B$ are given constants. In the majority of the paper, and unless otherwise stated, we will for (2.18*a*) assume the natural choice

$$\varrho_k = 0, \quad k = 1 \to I_B. \tag{2.19}$$

For more information on the conditions (2.15*a–c*) and (2.18*a,b*), with (2.19), we refer to [8], where one can also find the necessary techniques in order to show that (2.14) together with these conditions is a gradient flow of (2.10), i.e. that the total weighted surface area is monotonically decreasing in time. Similarly to (2.8*b*), we observe that for a fixed k, (2.18*a*) with (2.19) prescribes an angle of 90° between $\gamma'_{s_k}(\vec{\nu}_{s_k})$ and the normal of the external boundary $\partial\mathscr{D}_{d_k}$. Strictly speaking, this corresponds to a zero tangential forcing on the boundary (see e.g. [25, p. 102] for a discussion in the two-dimensional case). However, in cases where the phases separated by Γ_{s_k} have different contact energy densities with the external boundary $\partial\mathscr{D}_{d_k}$, something that is of interest in physical applications, a non-zero tangential forcing at the boundary needs to be considered. This corresponds to choosing $\varrho_k \neq 0$ in (2.18*a*), which for $|\varrho_k| \leqslant |\gamma'_{s_k}(\vec{\nu}_{s_k})|$ leads to a contact angle of $\arccos \frac{\varrho_k}{|\gamma'_{s_k}(\vec{\nu}_{s_k})|}$ between $\gamma'_{s_k}(\vec{\nu}_{s_k})$ and $\vec{n}_{d_k}$. In the isotropic case (2.12), this has a geometric interpretation, and we obtain, if $|\varrho_k| \leqslant \varsigma_{s_k}$, a contact angle of $\alpha_k = \arccos \frac{\varrho_k}{\varsigma_{s_k}}$ between Γ_{s_k} and $\partial\mathscr{D}_{d_k}$. See e.g. [24] for more details on the physical background of the conditions (2.18*a*) in the isotropic case (2.12). In fact, the conditions (2.18*a*) arise naturally on modifying the energy (2.10) appropriately, by adding to it a contribution from the external boundary intersection lines. In particular, we can prove Proposition 2.1, which shows that ϱ_k arises as the change in contact energy density in the direction of $-\vec{\nu}_{s_k}$, that the two phases separated by the interface Γ_{s_k} have with the external boundary $\partial\mathscr{D}_{d_k}$. It is convenient to first introduce the following notation. Let

$$\vec{\xi}_k := (\vec{n}_{d_k} \,.\, \vec{\nu}_{s_k})\, \vec{\mu}_{s_k} - (\vec{n}_{d_k} \,.\, \vec{\mu}_{s_k})\, \vec{\nu}_{s_k} \quad \text{on } \mathscr{B}_k, \quad k = 1 \to I_B. \tag{2.20}$$

We observe that $\vec{\xi}_k$ is normal to $\mathscr{B}_k$ and lies in the tangent plane of $\partial\mathscr{D}_{d_k}$. We also note

https://doi.org/10.1017/S0956792510000203 Published online by Cambridge University Press

that $\vec{\xi}_k$ is obtained through a 90° rotation of the external normal vector $\vec{n}_{d_k}$ in the plane spanned by $\vec{\nu}_{s_k}$ and $\vec{\mu}_{s_k}$, and that $(\vec{n}_{d_k}, \vec{\xi}_k)$ have the same orientation as $(\vec{\nu}_{s_k}, \vec{\mu}_{s_k})$.

Proposition 2.1 *Let $\{\Gamma(t)\}_{t\geqslant 0}$ be a family of surfaces which satisfy* (2.14)*, the attachment condition* (2.5*a*)*, the triple-junction conditions* (2.15*a–c*) *and the boundary conditions* (2.18*a,b*)*. We further assume that $\Gamma(t) \subset \overline{\mathscr{D}}$, $t \geqslant 0$. Then it holds that*

$$\frac{\mathrm{d}}{\mathrm{d}t}\left[E_\gamma(\Gamma) + \sum_{k=1}^{I_B}\left(\widehat{\varsigma}_k^+ \,|\mathscr{G}_k^+| + \widehat{\varsigma}_k^- \,|\mathscr{G}_k^-|\right)\right] \leqslant 0, \tag{2.21}$$

where $\widehat{\varsigma}_k^\pm \geqslant 0$ are the external boundaries' contact energy densities which are related to ϱ_k by $\varrho_k = \widehat{\varsigma}_k^+ - \widehat{\varsigma}_k^-$, $k = 1 \to I_B$. Here $\mathscr{G}_k := \partial\mathscr{D}_{d_k} \cap \partial\mathscr{D} \cap \mathbb{B}_R^3$, with $R > 0$ chosen sufficiently large, and $\overline{\mathscr{G}}_k = \overline{\mathscr{G}_k^+} \cup \overline{\mathscr{G}_k^-}$ with $\overline{\mathscr{G}_k^+} \cap \overline{\mathscr{G}_k^-} = \mathscr{B}_k$, such that $\vec{\xi}_k$ is the outer normal to $\mathscr{G}_k^-$ on $\mathscr{B}_k$. In addition, here and throughout the paper, as is common, the sum in (2.21) *is taken to be zero for $I_B = 0$.*

Proof It follows from Lemma 3.1 in [8] that

$$\frac{\mathrm{d}}{\mathrm{d}t}E_\gamma(\Gamma) = \sum_{i=1}^{3}\int_{\Gamma_i} \mathscr{V}_i\,\nabla_s\,.\,\gamma_i'(\vec{\nu}_i)\,\mathrm{d}\mathscr{H}^2 + \sum_{i=1}^{3}\int_{\partial\Gamma_i} \vec{x}_{i,t}\,.\,(\gamma_i(\vec{\nu}_i)\,\vec{\mu}_i - (\gamma_i'(\vec{\nu}_i)\,.\,\vec{\mu}_i)\,\vec{\nu}_i)\,\mathrm{d}\mathscr{H}^1, \tag{2.22}$$

where we recall that $\mathscr{V}_i = \vec{x}_{i,t}\,.\,\vec{\nu}_i$ is the normal velocity of Γ_i. In addition, a transport theorem for $\mathscr{G}_k^\pm \subset \partial\mathscr{D}_{d_k}$ (see e.g. [1] or [28, (2.9)]) yields that

$$\frac{\mathrm{d}}{\mathrm{d}t}\sum_{k=1}^{I_B}\left(\widehat{\varsigma}_k^+ \,|\mathscr{G}_k^+| + \widehat{\varsigma}_k^- \,|\mathscr{G}_k^-|\right) = \sum_{k=1}^{I_B}\left(\widehat{\varsigma}_k^+\int_{\partial\mathscr{G}_k^+}\widehat{\mathscr{V}}_k^+\,\mathrm{d}\mathscr{H}^1 + \widehat{\varsigma}_k^-\int_{\partial\mathscr{G}_k^-}\widehat{\mathscr{V}}_k^-\,\mathrm{d}\mathscr{H}^1\right), \tag{2.23}$$

where $\widehat{\mathscr{V}}_k^\pm$ is the normal velocity of the curve $\partial\mathscr{G}_k^\pm$, living on the manifold $\partial\mathscr{D}_{d_k}$, in the direction of its normal vector $\vec{\xi}_k^\pm$. Here $\vec{\xi}_k^\pm$ is the unique outer normal to $\mathscr{G}_k^\pm$ that lives in the tangent plane of $\partial\mathscr{D}_{d_k}$. Of course, the only non-zero contributions in the integrals in (2.23) come from integrating over $\mathscr{B}_k$. In addition, we have that $\vec{\xi}_k^\pm = \mp\vec{\xi}_k$ on $\mathscr{B}_k$. Hence (2.23) simplifies to

$$\begin{aligned}\frac{\mathrm{d}}{\mathrm{d}t}\sum_{k=1}^{I_B}\left(\widehat{\varsigma}_k^+ \,|\mathscr{G}_k^+| + \widehat{\varsigma}_k^- \,|\mathscr{G}_k^-|\right) &= \sum_{k=1}^{I_B}(-\widehat{\varsigma}_k^+ + \widehat{\varsigma}_k^-)\int_{\mathscr{B}_k}\vec{x}_{s_k,t}\,.\,\vec{\xi}_k\,\mathrm{d}\mathscr{H}^1\\ &= -\sum_{k=1}^{I_B}\varrho_k\int_{\mathscr{B}_k}\vec{x}_{s_k,t}\,.\,\vec{\xi}_k\,\mathrm{d}\mathscr{H}^1.\end{aligned} \tag{2.24}$$

Moreover, as in [8, Section 3], it follows from the triple-junction condition (2.15*a*) that the integrals over $\mathscr{T}$ in the second sum in (2.22) vanish, so that only the corresponding integrals over $\mathscr{B}_k$, $k = 1 \to I_B$, remain. In addition, on recalling (2.8*a*), (2.20), (2.11) and

https://doi.org/10.1017/S0956792510000203 Published online by Cambridge University Press

(2.18*a*), it holds on a fixed $\mathscr{B}_k$ that

$$\begin{aligned}
&\vec{x}_{s_k,t} \,.\, [\gamma_{s_k}(\vec{\nu}_{s_k})\,\vec{\mu}_{s_k} - (\gamma'_{s_k}(\vec{\nu}_{s_k}) \,.\, \vec{\mu}_{s_k})\,\vec{\nu}_{s_k}] \\
&\quad = (\vec{x}_{s_k,t} \,.\, \vec{\xi}_k)\,\vec{\xi}_k \,.\, [\gamma_{s_k}(\vec{\nu}_{s_k})\,\vec{\mu}_{s_k} - (\gamma'_{s_k}(\vec{\nu}_{s_k}) \,.\, \vec{\mu}_{s_k})\,\vec{\nu}_{s_k}] \\
&\quad = (\vec{x}_{s_k,t} \,.\, \vec{\xi}_k)\,\vec{\xi}_k \,.\, [(\gamma'_{s_k}(\vec{\nu}_{s_k}) \,.\, \vec{\nu}_{s_k})\,\vec{\mu}_{s_k} - (\gamma'_{s_k}(\vec{\nu}_{s_k}) \,.\, \vec{\mu}_{s_k})\,\vec{\nu}_{s_k}] \\
&\quad = (\vec{x}_{s_k,t} \,.\, \vec{\xi}_k)\,\vec{n}_{d_k} \,.\, \gamma'_{s_k}(\vec{\nu}_{s_k}) = \varrho_k\,(\vec{x}_{s_k,t} \,.\, \vec{\xi}_k),
\end{aligned} \tag{2.25}$$

where we have noted that the second vector on the left-hand side, similarly to (2.20), is a rotation through 90° of $\gamma'_{s_k}(\vec{\nu}_{s_k})$ in the plane spanned by $\vec{\nu}_{s_k}$ and $\vec{\mu}_{s_k}$. Hence it follows that

$$\begin{aligned}
\frac{\mathrm{d}}{\mathrm{d}t}\,E_\gamma(\Gamma) &= \sum_{i=1}^{3} \int_{\Gamma_i} \mathscr{V}_i\,\nabla_s \,.\, \gamma'_i(\vec{\nu}_i)\,\mathrm{d}\mathscr{H}^2 \\
&\quad + \sum_{i=1}^{I_B} \int_{\mathscr{B}_k} \vec{x}_{s_k,t} \,.\, (\gamma_{s_k}(\vec{\nu}_{s_k})\,\vec{\mu}_{s_k} - (\gamma'_{s_k}(\vec{\nu}_{s_k}) \,.\, \vec{\mu}_{s_k})\,\vec{\nu}_{s_k})\,\mathrm{d}\mathscr{H}^1 \\
&= \sum_{i=1}^{3} \int_{\Gamma_i} \mathscr{V}_i\,\nabla_s \,.\, \gamma'_i(\vec{\nu}_i)\,\mathrm{d}\mathscr{H}^2 + \varrho_k \int_{\mathscr{B}_k} \vec{x}_{s_k,t} \,.\, \vec{\xi}_k\,\mathrm{d}\mathscr{H}^1.
\end{aligned} \tag{2.26}$$

Combining (2.24) and (2.26) yields, on noting (2.14), (2.15*b*,*c*) and (2.18*b*) that

$$\begin{aligned}
&\frac{\mathrm{d}}{\mathrm{d}t}\left[E_\gamma(\Gamma) + \sum_{k=1}^{I_B} \left(\widehat{\varsigma}_k^{+}\,|\mathscr{G}_k^{+}| + \widehat{\varsigma}_k^{-}\,|\mathscr{G}_k^{-}|\right)\right] \\
&\quad = -\sum_{i=1}^{2} \int_{\Gamma_i} \beta_i(\vec{\nu}_i)\,|\nabla_s\,\varkappa_{\gamma,i}|^2\,\mathrm{d}\mathscr{H}^2 - \int_{\Gamma_3} \beta_3(\vec{\nu}_3)\,(\varkappa_{\gamma,3})^2\,\mathrm{d}\mathscr{H}^2 \leqslant 0,
\end{aligned} \tag{2.27}$$

which asserts the claim. □

As a consequence of Proposition 2.1, we observe that only the difference in $\widehat{\varsigma}_k^{\pm}$ is important for the gradient flow of the energy, and not their magnitudes. As a consequence, while $\widehat{\varsigma}_k^{\pm}$ uniquely determine ϱ_k, the converse is not true.

In the remainder of this section, we adopt the techniques in [8] in order to derive a weak formulation of the flow (2.14) with (2.5*a*), (2.15*a*–*c*) and (2.6), (2.18*a*,*b*). This weak formulation will form the basis of our finite-element approximation, which we will introduce in Section 3. To this end, and following our recent work in [7], we will restrict ourselves to anisotropic surface energy densities of the form

$$\gamma_i(\vec{p}) = \sum_{\ell=1}^{L_i} \gamma_i^{(\ell)}(\vec{p}), \quad \text{where} \quad \gamma_i^{(\ell)}(\vec{p}) := [\vec{p} \,.\, G_i^{(\ell)}\,\vec{p}]^{\frac{1}{2}}, \tag{2.28}$$

where $G_i^{(\ell)} \in \mathbb{R}^{3\times 3}$, $\ell = 1 \to L_i$ are symmetric and positive definite; $i = 1 \to 3$. This class of convex anisotropies leads to unconditionally stable numerical approximations (see Section 3). For example anisotropies that can be modelled by (2.28) we refer to [8] (see also [7]). Introducing a weak formulation of the flow (2.14) is mostly straightforward on

https://doi.org/10.1017/S0956792510000203 Published online by Cambridge University Press

suitably adapting the techniques introduced in [8]. The main novelty is how to incorporate the non-zero boundary conditions (2.18*a*). But in view of the proof of Proposition 2.1, this is also not difficult.

Let $\underline{V}(\Gamma) := \{(\vec{\chi}_1, \vec{\chi}_2, \vec{\chi}_3) \in \times_{i=1}^{3} H^1(\Gamma_i, \mathbb{R}^3) : \vec{\chi}_1 = \vec{\chi}_2 = \vec{\chi}_3 \ \text{ on } \mathscr{T}\}$ and

$$\underline{V}_{\partial}(\Gamma) := \{(\vec{\chi}_1, \vec{\chi}_2, \vec{\chi}_3) \in \underline{V}(\Gamma) : \vec{n}_{d_k} \cdot \vec{\chi}_{s_k} = 0 \ \text{ on } \mathscr{B}_k, \quad k = 1 \to I_B\}, \tag{2.29a}$$

$$W(\Gamma) := \{(\chi_1, \chi_2, \chi_3) \in \overset{3}{\underset{i=1}{\times}} H^1(\Gamma_i, \mathbb{R}) : \chi_1 + \chi_2 = 0 \ \text{ on } \mathscr{T}\}. \tag{2.29b}$$

Here and throughout $\Gamma = (\Gamma_1, \Gamma_2, \Gamma_3)$ with $\Gamma_i = \Gamma_i(t) = \vec{x}_i(\Omega_i, t)$, $i = 1 \to 3$; where $\vec{x}(\cdot, t) \in \underline{V}(\Omega)$ and

$$\underline{V}(\Omega) := \{(\vec{\chi}_1, \vec{\chi}_2, \vec{\chi}_3) \in \overset{3}{\underset{i=1}{\times}} H^1(\Omega_i, \mathbb{R}^3) : \vec{\chi}_1(\partial_{p_1}\Omega_1) = \vec{\chi}_2(\partial_{p_2}\Omega_2) = \vec{\chi}_3(\partial_{p_3}\Omega_3)\}. \tag{2.29c}$$

From now on, and throughout this paper, we will use the shorthand notation $\eta \in W(\Gamma)$ to mean $\eta = (\eta_1, \eta_2, \eta_3) \in W(\Gamma)$, and similarly for other functions and quantities defined on all surfaces Γ_i, $i = 1 \to 3$. In addition, for scalar, vector and tensor valued functions $\eta, \chi \in \overset{3}{\underset{i=1}{\times}} L^2(\Gamma_i, Y)$, with $Y = \mathbb{R}$, $\mathbb{R}^3$ or $\mathbb{R}^{3\times 3}$, we define the L^2 inner product $\langle \cdot, \cdot \rangle$ over Γ as follows

$$\langle \eta, \chi \rangle := \sum_{i=1}^{3} \int_{\Gamma_i} \eta_i \cdot \chi_i \, \mathrm{d}\mathscr{H}^2. \tag{2.30}$$

Moreover, let

$$\langle \nabla_s^{\widetilde{G}} \vec{\eta}, \nabla_s^{\widetilde{G}} \vec{\chi} \rangle_\gamma := \sum_{i=1}^{3} \sum_{\ell=1}^{L_i} \int_{\Gamma_i} \left(\nabla_s^{\widetilde{G}_i^{(\ell)}} \vec{\eta}_i, \nabla_s^{\widetilde{G}_i^{(\ell)}} \vec{\chi}_i \right)_{\widetilde{G}_i^{(\ell)}} \gamma_i^{(\ell)}(\vec{\nu}_i) \, \mathrm{d}\mathscr{H}^2, \tag{2.31}$$

where $\widetilde{G}_i^{(\ell)} := [\det G_i^{(\ell)}]^{\frac{1}{2}} \, [G_i^{(\ell)}]^{-1}$, $\ell = 1 \to L_i$, $i = 1 \to 3$, and the anisotropic tangential gradient operators $\nabla_s^{\widetilde{G}_i^{(\ell)}}$ as well as the inner products $(\cdot, \cdot)_{\widetilde{G}_i^{(\ell)}}$ are defined in [7] (see also [8]). With these definitions, the following representations of the anisotropic curvature vectors can be obtained (see [7] for details):

$$\varkappa_{\gamma,i} \, \vec{\nu}_i = \sum_{\ell=1}^{L_i} \gamma_i^{(\ell)}(\vec{\nu}_i) \, \widetilde{G}_i^{(\ell)} \, \nabla_s^{\widetilde{G}_i^{(\ell)}} \cdot \left[\nabla_s^{\widetilde{G}_i^{(\ell)}} \, \vec{x}_i \right], \quad i = 1 \to 3. \tag{2.32}$$

Of course, in the isotropic case (2.12) with $\varsigma = (1, 1, 1)$, the identities (2.32) collapse to (2.1). We note that the shorthand notation $\langle \nabla_s^{\widetilde{G}} \cdot, \nabla_s^{\widetilde{G}} \cdot \rangle_\gamma$ defined in (2.31) is the natural cluster analogue of the inner product defined in [7].

For later reference, we quote the following result from [8].

Lemma 2.1 *Let γ be given by* (2.28) *and let $\vec{g} \in \underline{V}(\Gamma)$ be a smooth vector field. Then it holds that*

$$\left\langle \nabla_s^{\widetilde{G}} \vec{x}, \nabla_s^{\widetilde{G}} \vec{g} \right\rangle_\gamma = -\langle \varkappa_\gamma \, \vec{\nu}, \vec{g} \rangle + \sum_{i=1}^{3} \int_{\partial\Gamma_i} \vec{g} \cdot (\gamma_i(\vec{\nu}_i) \, \vec{\mu}_i - (\gamma_i'(\vec{\nu}_i) \cdot \vec{\mu}_i) \, \vec{\nu}_i) \, \mathrm{d}\mathscr{H}^1. \tag{2.33}$$

https://doi.org/10.1017/S0956792510000203 Published online by Cambridge University Press

Proof In the proof of Lemma 3.3 in [8] it is shown that

$$\left\langle \nabla_s^{\widetilde{G}}\,\vec{x}, \nabla_s^{\widetilde{G}}\,\vec{g} \right\rangle_\gamma = \sum_{i=1}^{3} \int_{\Gamma_i} (\vec{g}\,.\,\vec{\nu}_i)\,\nabla_s\,.\,\gamma_i'(\vec{\nu}_i)\,\mathrm{d}\mathscr{H}^2 + \sum_{i=1}^{3} \int_{\partial\Gamma_i} \vec{g}\,.\,(\gamma_i(\vec{\nu}_i)\,\vec{\mu}_i - (\gamma_i'(\vec{\nu}_i)\,.\,\vec{\mu}_i)\,\vec{\nu}_i)\,\mathrm{d}\mathscr{H}^1. \tag{2.34}$$

Now the desired result (2.33) follows on noting (2.13*a,b*). We observe that the result (2.34) can be derived by multiplying the identities (2.32) with $\vec{g}$, noting (2.13*a,b*), integrating over Γ and performing integration by parts, on utilising and extending the techniques presented in [7] (see [8]). □

We now introduce the weak formulation of (2.14) together with (2.5*a*), (2.15*a–c*) and (2.6), (2.18*a,b*). Following [8], we reformulate (2.14) as

$$[\vec{x}_i]_t\,.\,\vec{\nu}_i = -\nabla_s\,.\,(\beta_i(\vec{\nu}_i)\,\nabla_s\,\varkappa_{\gamma,i}),\ \ i = 1 \to 2, \quad [\vec{x}_3]_t\,.\,\vec{\nu}_3 = \beta_3(\vec{\nu}_3)\,\varkappa_{\gamma,3} \tag{2.35}$$

and (2.32). Then multiplying the three equations in (2.35) with a test function $\eta \in W(\Gamma)$ and the three equations in (2.32) with a test function $\vec{\chi} \in \underline{V}_{\partial}(\Gamma)$, integrating over Γ, noting (2.33), (2.15*a–c*) and (2.18*a,b*) and using a similar argument to (2.25), we obtain the following weak formulation: Find $\vec{x} \in \underline{V}(\Omega)$ satisfying (2.8*a*) and $\varkappa_\gamma \in W(\Gamma)$ such that

$$\langle \vec{x}_t, \eta\,\vec{\nu}\rangle - \langle \varkappa_\gamma, \eta\rangle_\beta^\star = 0 \quad \forall\ \eta \in W(\Gamma), \tag{2.36a}$$

$$\langle \varkappa_\gamma\,\vec{\nu}, \vec{\chi}\rangle + \langle \nabla_s^{\widetilde{G}}\,\vec{x}, \nabla_s^{\widetilde{G}}\,\vec{\chi}\rangle_\gamma = \sum_{k=1}^{I_B} \int_{\mathscr{B}_k} \varrho_k\,\vec{\xi}_k\,.\,\vec{\chi}_{s_k}\,\mathrm{d}\mathscr{H}^1 \quad \forall\ \vec{\chi} \in \underline{V}_{\partial}(\Gamma), \tag{2.36b}$$

where we recall the definitions (2.20) and (2.31), and where

$$\langle \eta, \chi\rangle_\beta^\star := \sum_{i=1}^{2} \int_{\Gamma_i} \beta_i(\vec{\nu}_i)\,\nabla_s\,\eta_i\,.\,\nabla_s\,\chi_i\,\mathrm{d}\mathscr{H}^2 + \int_{\Gamma_3} \beta_3(\vec{\nu}_3)\,\eta_3\,\chi_3\,\mathrm{d}\mathscr{H}^2. \tag{2.37}$$

We observe that in the formulation (2.36*a,b*) the conditions (2.15*a,b*) and (2.18*a,b*) are formulated weakly, while the remaining conditions are enforced strongly through the trial spaces; recall (2.29*a,b*). Furthermore, we note for the reader's convenience that for isotropic energies (2.12) with constant mobilities $\beta = (1, 1, 1)$, the strong formulation (2.35), (2.32) reduces to

$$[\vec{x}_i]_t\,.\,\vec{\nu}_i = -\varsigma_i \Delta_s \varkappa_i,\ \ i = 1 \to 2, \quad [\vec{x}_3]_t\,.\,\vec{\nu}_3 = \varsigma_3\,\varkappa_3 \quad \text{and} \quad \varkappa_i\,\vec{\nu}_i = \Delta_s\,\vec{x}_i,\ \ i = 1 \to 3, \tag{2.38}$$

while the weak formulation (2.36*a,b*) collapses to: Find $\vec{x} \in \underline{V}(\Omega)$ satisfying (2.8*a*) and

https://doi.org/10.1017/S0956792510000203 Published online by Cambridge University Press

$\varkappa_\gamma \equiv \varsigma\,\varkappa \in W(\Gamma)$ such that

$$\langle \vec{x}_t, \eta\,\vec{\nu}\rangle - \langle \varsigma\,\varkappa, \eta\rangle^\star = 0 \quad \forall\ \eta \in W(\Gamma), \tag{2.39a}$$

$$\langle \varsigma\,\varkappa\,\vec{\nu}, \vec{\chi}\rangle + \langle \varsigma\,\nabla_s\,\vec{x}, \nabla_s\,\vec{\chi}\rangle = \sum_{k=1}^{I_B} \int_{\mathscr{B}_k} \varrho_k\,\vec{\xi}_k \cdot \vec{\chi}_{s_k}\,\mathrm{d}\mathscr{H}^1 \quad \forall\ \vec{\chi} \in \underline{V}_\partial(\Gamma), \tag{2.39b}$$

where $\langle \eta, \chi\rangle^\star := \sum_{i=1}^2 \int_{\Gamma_i} \nabla_s\,\eta_i \cdot \nabla_s\,\chi_i\,\mathrm{d}\mathscr{H}^2 + \int_{\Gamma_3} \eta_3\,\chi_3\,\mathrm{d}\mathscr{H}^2$.

3 Parametric finite-element approximation

In this section, we consider a finite-element approximation for the mixed flow (2.14). In particular, on utilising and extending the techniques recently introduced in [8], we will introduce the natural finite-element analogue of the weak formulation (2.36*a*,*b*).

For $i \to 3$, let Ω_i^h be a triangulation approximating $\overline{\Omega}_i \subset \mathbb{R}^2$, so that $\Omega_i^h = \cup_{j=1}^{J_i} \overline{\sigma_j^i}$, where $\{\sigma_j^i\}_{j=1}^{J_i}$ is a family of mutually disjoint open triangles with vertices $\{\vec{q}_k^{\,i}\}_{k=1}^{K_i}$. In particular, let $\{\vec{q}_k^{\,i}\}_{k=1}^{\overline{K}_i}$ denote the vertices in the interior of Ω_i^h and let $\{\vec{q}_k^{\,i}\}_{k=\overline{K}_i+1}^{K_i}$ denote the vertices on $\partial\Omega_i^h$. We set $h := \max_{i=1\to 3} \max_{j=1\to J_i} \mathrm{diam}(\sigma_j^i)$. We introduce the finite-element space $\underline{\widehat{V}}^h(\Omega^h) := \{\vec{\chi} \in \overset{3}{\underset{i=1}{\times}} C(\Omega_i^h, \mathbb{R}^3) : \vec{\chi}_i\,|_{\sigma_j^i}$ is linear $\forall\ j = 1 \to J_i,\ i = 1 \to 3\}$. Let $\partial_j\Omega_i^h$ be the polygonal curve approximating $\overline{\partial_j\Omega_i}$, $j = 1 \to I_P^i$, $i = 1 \to 3$. We assume that the endpoints of $\partial_j\Omega_i^h$ and $\overline{\partial_j\Omega_i}$ coincide and that

$$Z := \#\left\{\{\vec{q}_l^{\,1}\}_{l=1}^{K_1} \cap \partial_{p_1}\Omega_1^h\right\} = \#\left\{\{\vec{q}_l^{\,2}\}_{l=1}^{K_2} \cap \partial_{p_2}\Omega_2^h\right\} = \#\left\{\{\vec{q}_l^{\,3}\}_{l=1}^{K_3} \cap \partial_{p_3}\Omega_3^h\right\}. \tag{3.1}$$

In addition, let

$$\vec{\rho}_i : \{1 \to Z\} \to \left\{\{\vec{q}_l^{\,i}\}_{l=1}^{K_i} \cap \partial_{p_i}\Omega_i^h\right\}, \quad i = 1 \to 3, \tag{3.2}$$

be a bijective map such that $(\vec{\rho}_i(1), \ldots, \vec{\rho}_i(Z))$ is an ordered sequence of vertices of the polygonal curve $\partial_{p_i}\Omega_i^h$, $i = 1 \to 3$. Then we define the natural discrete analogue of $\underline{V}(\Omega)$ by $\underline{V}^h(\Omega^h) := \{\vec{\chi} \in \underline{\widehat{V}}^h(\Omega^h) : \vec{\chi}_1(\vec{\rho}_1(l)) = \vec{\chi}_2(\vec{\rho}_2(l)) = \vec{\chi}_3(\vec{\rho}_3(l)),\ l = 1 \to Z\}$.

Let $0 = t_0 < t_1 < \ldots < t_{M-1} < t_M = T$ be a partitioning of $[0, T]$ into possibly variable time steps $\tau_m := t_{m+1} - t_m$, $m = 0 \to M-1$. The surfaces Γ_i^m are now given by their parameterisations $\vec{X}_i^m$, $i = 1 \to 3$, where $\vec{X}^m \in \underline{V}^h(\Omega^h)$. We set $\Gamma^m := \vec{X}^m(\Omega^h)$ and observe that, with the above definitions, the polygonal curve $\mathscr{T}^m$ defined by the ordered sequence of vertices $(\vec{X}_1^m(\vec{\rho}_1(1)), \ldots, \vec{X}_1^m(\vec{\rho}_1(Z)))$, is the triple-junction line of the polyhedral surface cluster Γ^m. Similarly, let the polygonal curves $\mathscr{B}_k^m$ be given by an appropriately defined ordering of the vertices $\{\vec{X}_{s_k}^m(\vec{q}) : \vec{q} \in \{\vec{q}_l^{\,s_k}\}_{l=1}^{K_{s_k}} \cap \partial_{p_k}\Omega_{s_k}^h\}$, $k = 1 \to I_B$, so that $\mathscr{B}_k^m$ are the boundary intersection lines of Γ^m, i.e. the natural discrete analogues of $\mathscr{B}_k$, $k = 1 \to I_B$.

In addition, let $\partial\mathscr{D}_j$, $j = 1 \to I_D$, be given by functions $F_j \in C^1(\mathbb{R}^3)$ such that

$$\partial\mathscr{D}_j = \{\vec{z} \in \mathbb{R}^3 : F_j(\vec{z}) = 0\} \quad \text{and} \quad |\nabla F_j(\vec{z})| = 1 \quad \forall\ \vec{z} \in \partial\mathscr{D}_j, \quad j = 1 \to I_D. \tag{3.3}$$

For example, if D_j is the slab domain $(0,1) \times \mathbb{R}^2$, then a possible definition for this function is $F_j(\vec{z}) = z_1\,(z_1 - 1)$.

We are now in a position to define the necessary finite-element spaces on Γ^m. Let $\sigma_j^{m,i} := \vec{X}_i^m(\sigma_j^i)$ and similarly $\vec{q}_k^{\,m,i} := \vec{X}_i^m(\vec{q}_k^{\,i})$. First we introduce piecewise linear finite

https://doi.org/10.1017/S0956792510000203 Published online by Cambridge University Press

elements on Γ^m by

$$\begin{aligned}\underline{\widehat{V}}^h(\Gamma^m) &:= \{\vec{\chi} \in \mathop{\times}_{i=1}^{3} C(\Gamma_i^m, \mathbb{R}^3) : \vec{\chi}_i|_{\sigma_j^{m,i}} \text{ is linear } \forall\ j = 1 \to J_i,\ i = 1 \to 3\} \\ &=: [\widehat{W}^h(\Gamma^m)]^3, \end{aligned} \tag{3.4}$$

where $\widehat{W}^h(\Gamma^m) \subset \mathop{\times}_{i=1}^{3} H^1(\Gamma_i^m, \mathbb{R})$ is the space of scalar continuous piecewise linear functions on Γ^m, with $\{\{\phi_k^{m,i}\}_{k=1}^{K_i}\}_{i=1}^3$ denoting the standard basis of $\widehat{W}^h(\Gamma^m)$, i.e. $\phi_l^{m,i}(\vec{q}_k^{\,m,j}) = \delta_{ij}\,\delta_{kl}$ for all $l = 1 \to K_i$, $k = 1 \to K_j$, $i, j = 1 \to 3$. Then $\underline{V}_{\partial}^h(\Gamma^m)$ and $W^h(\Gamma^m)$, the natural discrete analogues of $\underline{V}_{\partial}(\Gamma)$ and $W(\Gamma)$, are defined by

$$\begin{aligned}\underline{V}_{\partial}^h(\Gamma^m) := \{\vec{\chi} \in \underline{\widehat{V}}^h(\Gamma^m) : \vec{\chi}_1 = \vec{\chi}_2 = \vec{\chi}_3 \ \text{ on } \mathscr{T}^m, \\ \nabla F_{d_k}(\vec{q}\,).\,\vec{\chi}_{s_k}(\vec{q}\,) = 0 \quad \forall\ \vec{q} \in \widehat{\mathscr{B}}_k^m, \quad k = 1 \to I_B\} \end{aligned} \tag{3.5a}$$

$$\text{and} \quad W^h(\Gamma^m) := \{\chi \in \widehat{W}^h(\Gamma^m) : \chi_1 + \chi_2 = 0 \ \text{ on } \mathscr{T}^m\}, \tag{3.5b}$$

where for notational convenience we define $\widehat{\mathscr{B}}_k^m := \mathscr{B}_k^m \cap \{\vec{q}_l^{\,m,s_k}\}_{l=1}^{K_{s_k}}$, $k = 1 \to I_B$, and where in (3.5*a*) we recall (3.3). We note that the above definitions imply that $\vec{X}^m = \mathrm{id}\,|_{\Gamma^m} \in \underline{V}^h(\Gamma^m) := \{\vec{\chi} \in \underline{\widehat{V}}^h(\Gamma^m) : \vec{\chi}_1 = \vec{\chi}_2 = \vec{\chi}_3 \ \text{ on } \mathscr{T}^m\}$ on Γ^m and that, if $\vec{X}^{m+1} \in \underline{V}^h(\Gamma^m)$, then $\Gamma^{m+1} = \vec{X}^{m+1}(\Gamma^m)$ can be parameterised with a function from $\underline{V}^h(\Omega^h)$, which we will also denote by $\vec{X}^{m+1}$.

Similarly to (2.30), we introduce the L^2 inner product $\langle\cdot,\cdot\rangle_m$ over the current polyhedral surface cluster Γ^m, which is described by the vector function $\vec{X}^m$, as follows:

$$\langle u, v\rangle_m := \sum_{i=1}^{3} \langle u_i, v_i\rangle_{m,i} := \sum_{i=1}^{3} \int_{\Gamma_i^m} u_i\,.\,v_i \,\mathrm{d}\mathscr{H}^2. \tag{3.6a}$$

If u, v are piecewise continuous, with possible jumps across the edges of $\{\sigma_j^{m,i}\}_{j=1}^{J_i}$, $i = 1 \to 3$, we introduce the mass lumped inner product $\langle\cdot,\cdot\rangle_m^h$ as

$$\langle u, v\rangle_m^h := \sum_{i=1}^{3} \langle u_i, v_i\rangle_{m,i}^h := \sum_{i=1}^{3} \sum_{j=1}^{J_i} \tfrac{1}{3}\,|\sigma_j^{m,i}| \sum_{k=0}^{2} \lim_{\sigma_j^{m,i} \ni \vec{p} \to \vec{q}_{j_k}^{\,m,i}} (u_i\,.\,v_i)(\vec{p}), \tag{3.6b}$$

where $\{\vec{q}_{j_k}^{\,m,i}\}_{k=0}^2$ are the vertices of $\sigma_j^{m,i}$. Here $|\sigma_j^{m,i}| = \frac{1}{2}\,|(\vec{q}_{j_1}^{\,m,i} - \vec{q}_{j_0}^{\,m,i}) \wedge (\vec{q}_{j_2}^{\,m,i} - \vec{q}_{j_0}^{\,m,i})|$ is the area of $\sigma_j^{m,i}$. Combining the definitions (3.6*a*,*b*) we also introduce the inner product $\langle\cdot,\cdot\rangle_m^{\star,h}$ by

$$\langle u, v\rangle_m^{\star,h} := \sum_{i=1}^{2} \langle \nabla_s\, u_i, \nabla_s\, v_i\rangle_{m,i} + \langle u_3, v_3\rangle_{m,3}^h. \tag{3.6c}$$

In addition, we introduce the unit normal $\vec{\nu}_i^m$ to Γ_i^m; that is,

$$\vec{\nu}_{i,j}^m := \vec{\nu}_i^m\,|_{\sigma_j^{m,i}} := \frac{(\vec{q}_{j_1}^{\,m,i} - \vec{q}_{j_0}^{\,m,i}) \wedge (\vec{q}_{j_2}^{\,m,i} - \vec{q}_{j_0}^{\,m,i})}{|(\vec{q}_{j_1}^{\,m,i} - \vec{q}_{j_0}^{\,m,i}) \wedge (\vec{q}_{j_2}^{\,m,i} - \vec{q}_{j_0}^{\,m,i})|},$$

where we have assumed that the vertices $\{\vec{q}_{j_k}^{\,m,i}\}_{k=0}^2$ are ordered with the same orientation

https://doi.org/10.1017/S0956792510000203 Published online by Cambridge University Press

for all $\sigma_j^{m,i}$, $j = 1 \to J_i$. Now the natural discrete analogues of (2.37) and (2.31) are defined by

$$\langle u, v \rangle_{\beta,m}^{\star,h} := \sum_{i=1}^{2} \left\langle \beta_i\big(\vec{v}_i^{\,m}\big)\, \nabla_s u_i, \nabla_s v_i \right\rangle_{m,i} + \left\langle \beta_3\big(\vec{v}_3^{\,m}\big)\, u_3, v_3 \right\rangle_{m,3}^{h}$$

and

$$\begin{aligned} \left\langle \nabla_s^{\widetilde{G}}\, \vec{\eta}, \nabla_s^{\widetilde{G}}\, \vec{\chi} \right\rangle_{\gamma,m} &:= \sum_{i=1}^{3} \left\langle \nabla_s^{\widetilde{G}_i}\, \vec{\eta}_i, \nabla_s^{\widetilde{G}_i}\, \vec{\chi}_i \right\rangle_{\gamma_i,m,i} \\ &:= \sum_{i=1}^{3} \sum_{\ell=1}^{L_i} \int_{\Gamma_i^m} \left(\nabla_s^{\widetilde{G}_i^{(\ell)}}\, \vec{\eta}_i, \nabla_s^{\widetilde{G}_i^{(\ell)}}\, \vec{\chi}_i \right)_{\widetilde{G}_i^{(\ell)}} \gamma_i^{(\ell)}\big(\vec{v}_i^{\,m}\big)\, \mathrm{d}\mathscr{H}^2, \end{aligned} \tag{3.7}$$

respectively. Finally, we introduce the discrete analogues of (2.20). To this end, let $\vec{b}_{k,j}^{\,m}$ denote the barycentre of $\overline{\sigma_j^{m,s_k}} \cap \mathscr{B}_k^m$, $j = 1 \to J_{s_k}$, $k = 1 \to I_B$. For notational simplicity we let $\vec{0}$ be the barycentre of the empty set. Then we define

$$\vec{\xi}_{k,j}^{\,m} := \vec{\xi}_k^{\,m}\,|_{\overline{\sigma_j^{m,s_k}} \cap \mathscr{B}_k^m} = \left(\left[\frac{\nabla F_{d_k}(\vec{b}_{k,j}^{\,m})}{|\nabla F_{d_k}(\vec{b}_{k,j}^{\,m})|} \cdot \vec{\nu}_{s_k}^{\,m} \right] \vec{\mu}_{s_k}^{\,m} - \left[\frac{\nabla F_{d_k}(\vec{b}_{k,j}^{\,m})}{|\nabla F_{d_k}(\vec{b}_{k,j}^{\,m})|} \cdot \vec{\mu}_{s_k}^{\,m} \right] \vec{\nu}_{s_k}^{\,m} \right) |_{\overline{\sigma_j^{m,s_k}} \cap \mathscr{B}_k^m} \tag{3.8}$$

for all $j = 1 \to J_{s_k}$ with $\overline{\sigma_j^{m,s_k}} \cap \mathscr{B}_k^m \neq \emptyset$, $k = 1 \to I_B$. Here $\vec{\mu}_{s_k}^{\,m}$ denotes the conormal of $\Gamma_{s_k}^m$. Of course, in the case of flat boundaries $\partial\mathscr{D}_{d_k}$, the vector $\vec{\xi}_k^{\,m}$ reduces to the standard normal vector to the polygonal curve $\mathscr{B}_k^m$ within the hyperplane $\partial\mathscr{D}_{d_k}$, and so it can be computed in a simpler fashion, using only information on $\mathscr{B}_k^m$ and $\vec{n}_{d_k}$.

We propose the following finite-element approximation of (2.14) with (2.5*a*), (2.15*a–c*) and (2.8*a*), (2.18*a,b*); based on the equivalent weak formulation (2.36*a,b*). Find $\delta\vec{X}^{m+1} \in \underline{V}_{\partial}^h(\Gamma^m)$ and $\kappa_\gamma^{m+1} \in W^h(\Gamma^m)$, where $\vec{X}^{m+1} := \vec{X}^m + \delta\vec{X}^{m+1}$, such that

$$\left\langle \frac{\delta\vec{X}^{m+1}}{\tau_m}, \chi\, \vec{\nu}^m \right\rangle_m^h - \left\langle \kappa_\gamma^{m+1}, \chi \right\rangle_{\beta,m}^{\star,h} = 0 \quad \forall\ \chi \in W^h(\Gamma^m), \tag{3.9a}$$

$$\left\langle \kappa_\gamma^{m+1}\, \vec{\nu}^m, \vec{\eta} \right\rangle_m^h + \left\langle \nabla_s^{\widetilde{G}}\, \vec{X}^{m+1}, \nabla_s^{\widetilde{G}}\, \vec{\eta} \right\rangle_{\gamma,m} = \sum_{k=1}^{I_B} \int_{\mathscr{B}_k^m} \varrho_k\, \vec{\xi}_k^{\,m} \cdot \vec{\eta}_{s_k}\, \mathrm{d}\mathscr{H}^1 \quad \forall\ \vec{\eta} \in \underline{V}_{\partial}^h(\Gamma^m). \tag{3.9b}$$

Of course, in the case that $I_B = 0$, or if (2.19) holds, then the right-hand side in (3.9*b*) vanishes. We observe that, similarly to the formulation (2.36*a,b*), the conditions (2.15*a,b*) and (2.18*a,b*) are approximated weakly, while the conditions (2.5*a*) and (2.15*c*) are enforced strongly through the discrete trial spaces; recall (3.5*a,b*). For example, the angle condition (2.15*a*) at the triple-junction line, recall (2.16a), does not have to be prescribed explicitly. Instead, it will be satisfied in a weak sense by the finite-element solution $\vec{X}^{m+1}$, and in practice we observe that in general it is approximately satisfied. This is a common feature of variational approximation methods for such problems. In addition, we note that a linearised approximation of (2.8*a*) is enforced strongly via $\delta\vec{X}^{m+1} \in \underline{V}_{\partial}^h(\Gamma^m)$, so that the conditions (2.6) are enforced in a weak sense. In particular, for curved boundaries $\partial\mathscr{D}_{d_k}$

https://doi.org/10.1017/S0956792510000203 Published online by Cambridge University Press

the equations

$$F_{d_k}\big(\vec{X}^{m+1}_{s_k}\big) = 0 \quad \text{on } \partial_{p_k}\Omega^h_{s_k}, \quad k = 1 \to I_B, \tag{3.10}$$

are only approximately satisfied (see e.g. [2] for more details in the planar isotropic case). However, in this paper we restrict our numerical results to flat boundaries $\partial\mathscr{D}_{d_k}$ only. In this case, the constraints (3.10) are satisfied exactly by the solution $\vec{X}^{m+1}$ of (3.9*a*,*b*).

Remark 3.1 (The isotropic case) We note that the scheme (3.9*a*,*b*) in the isotropic case (2.12) can be equivalently formulated as follows. Find $\delta\vec{X}^{m+1} \in \underline{V}^h_{\vec{0}}(\Gamma^m)$ and $\kappa^{m+1} \in \widehat{W}^h(\Gamma^m)$, where $\vec{X}^{m+1} := \vec{X}^m + \delta\vec{X}^{m+1}$, such that $\varsigma\,\kappa^{m+1} \in W^h(\Gamma^m)$ and

$$\left\langle \frac{\delta\vec{X}^{m+1}}{\tau_m}, \chi\,\vec{\nu}^m \right\rangle^h_m - \langle \varsigma\,\kappa^{m+1}, \chi\rangle^{\star,h}_{\beta,m} = 0 \quad \forall\ \chi \in W^h(\Gamma^m), \tag{3.11a}$$

$$\langle \varsigma\,\kappa^{m+1}\,\vec{\nu}^m, \vec{\eta}\rangle^h_m + \langle \varsigma\,\nabla_s\,\vec{X}^{m+1}, \nabla_s\,\vec{\eta}\rangle_m = \sum_{k=1}^{I_B} \int_{\mathscr{B}^m_k} \varrho_k\,\vec{\xi}^m_k \cdot \vec{\eta}_{s_k}\,\mathrm{d}\mathscr{H}^1 \quad \forall\ \vec{\eta} \in \underline{V}^h_{\vec{0}}(\Gamma^m). \tag{3.11b}$$

Observe that only standard surface gradients and inner products appear in (3.11*a*,*b*), as is to be expected. Of course, in the case of constant mobilities $\beta = (1,1,1)$, the scheme (3.11*a*,*b*) is the natural finite-element approximation of (2.39*a*,*b*).

We now prove existence and uniqueness for a solution to (3.9*a*,*b*), which follow from a straightforward adaptation of the proofs given in [8]. To this end, we make the following very mild assumption on the triangulations at each time level.

($\mathscr{A}$) We assume for $m = 0 \to M$ that $|\sigma^{m,i}_j| = |\vec{X}^m_i(\sigma^i_j)| > 0$, $j = 1 \to J_i$, $i = 1 \to 3$.
For $k = 1 \to K_i$, let $\Xi^{m,i}_k := \{\sigma^{m,i}_j : \vec{q}^{\,m,i}_k \in \overline{\sigma^{m,i}_j}\}$ and set

$$\Lambda^{m,i}_k := \bigcup_{\sigma^{m,i}_j \in \Xi^{m,i}_k} \overline{\sigma^{m,i}_j} \quad \text{and} \quad \vec{\omega}^m_{i,k} := \frac{1}{|\Lambda^{m,i}_k|} \sum_{\sigma^i_j \in \Xi^{m,i}_k} |\sigma^{m,i}_j|\,\vec{\nu}^m_{i,j}.$$

Then we assume further that for $i = 1 \to 2$ there exists a $k \in \{1,\dots,\overline{K}_i\}$ such that $\vec{\omega}^m_{i,k} \neq \vec{0}$ and that $\dim \operatorname{span} U^m = 3$, $m = 0 \to M-1$, where $U^m := \{\{\vec{\omega}^m_{i,k}\}^{\overline{K}_i}_{k=1}\}^3_{i=1} \cup \{\{\nabla F_{d_k}(\vec{q})\}_{\vec{q}\in\widehat{\mathscr{B}}^m_k}\}^{I_B}_{k=1}$.

We stress that ($\mathscr{A}$) is a very weak assumption. It merely states that (a) the triangles of the polyhedral surface cluster Γ^m have positive area; that (b) on each of the two material boundaries Γ^m_i, $i = 1 \to 2$, at least one inner vertex normal $\vec{\omega}^m_{i,k}$ is non-zero; and that (c) among all the inner vertex normals $\vec{\omega}^m_{i,k}$ and all the boundary constraint vectors $\nabla F_{d_k}(\vec{q})$ there are three linearly independent vectors. The latter condition is only violated in very pathological cases, e.g. when the three surfaces overlap identically on a flat external boundary, and it never occurred in practice.

Theorem 3.1 *Let the assumption* ($\mathscr{A}$) *hold. Then there exists a unique solution* $(\delta\vec{X}^{m+1}, \kappa^{m+1}_\gamma) \in \underline{V}^h_{\vec{0}}(\Gamma^m) \times W^h(\Gamma^m)$ *to* (3.9*a*,*b*).

https://doi.org/10.1017/S0956792510000203 Published online by Cambridge University Press

Proof As (3.9*a*,*b*) is linear, existence follows from uniqueness. To investigate the latter, we consider the system: Find $\{\vec{X}, \kappa_\gamma\} \in \underline{V}_{\vec{0}}^h(\Gamma^m) \times W^h(\Gamma^m)$ such that

$$\langle \vec{X}, \chi\, \vec{v}^m \rangle_m^h - \tau_m \langle \kappa_\gamma, \chi \rangle_{\beta,m}^{\star,h} = 0 \quad \forall\ \chi \in W^h(\Gamma^m), \tag{3.12a}$$

$$\langle \kappa_\gamma\, \vec{v}^m, \vec{\eta} \rangle_m^h + \left\langle \nabla_s^{\widetilde{G}}\, \vec{X}, \nabla_s^{\widetilde{G}}\, \vec{\chi} \right\rangle_{\gamma,m} = 0 \quad \forall\ \vec{\eta} \in \underline{V}_{\vec{0}}^h(\Gamma^m). \tag{3.12b}$$

Choosing $\chi = \kappa_\gamma \in W^h(\Gamma^m)$ in (3.12*a*) and $\vec{\eta} = \vec{X} \in \underline{V}_{\vec{0}}^h(\Gamma^m)$ in (3.12*b*) yields that

$$\sum_{i=1}^{3} \sum_{\ell=1}^{L_i} \int_{\Gamma_i^m} \left(\nabla_s^{\widetilde{G}_i^{(\ell)}}\, \vec{X}_i, \nabla_s^{\widetilde{G}_i^{(\ell)}}\, \vec{X}_i \right)_{\widetilde{G}_i^{(\ell)}} \gamma_i^{(\ell)}(\vec{v}_i^m)\ \mathrm{d}\mathscr{H}^2$$
$$+ \tau_m \sum_{i=1}^{2} \langle \beta_i(\vec{v}_i^m)\, \nabla_s \kappa_{\gamma,i}, \nabla_s \kappa_{\gamma,i} \rangle_{m,i} + \tau_m \langle \beta_3(\vec{v}_3^m)\, \kappa_{\gamma,3}, \kappa_{\gamma,3} \rangle_{m,3}^h = 0. \tag{3.13}$$

Similarly to the proof of [8, Theorem 4.3], it follows from (3.13), the positive definiteness of $\widetilde{G}_i^{(\ell)}$, $\ell = 1 \to L_i$, $i = 1 \to 3$, and the positivity of β that $\kappa_{\gamma,i} = \kappa_i^c \in \mathbb{R}$, $i = 1 \to 3$, with $\kappa_1^c + \kappa_2^c = 0 = \kappa_3^c$; and, on noting $\vec{X} \in \underline{V}_{\vec{0}}^h(\Gamma^m)$ and the connectedness of Γ^m that $\vec{X}_i \equiv \vec{X}^c \in \mathbb{R}^3$, $i = 1 \to 3$. Hence

$$0 = \langle \kappa^c\, \vec{v}^m, \vec{\eta} \rangle_m^h \equiv \langle \kappa^c\, \vec{\omega}^m, \vec{\eta} \rangle_m^h \quad \forall\ \vec{\eta} \in \underline{V}_{\vec{0}}^h(\Gamma^m), \tag{3.14}$$

where $\vec{\omega}^m \in \underline{\widehat{V}}^h(\Gamma^m)$ with $\vec{\omega}_i^m(\vec{q}_k^{m,i}) = \vec{\omega}_{i,k}^m$, $k = 1 \to K_i$, $i = 1 \to 3$. Now (3.14) implies that $\kappa_i^c = 0$, $i = 1 \to 2$. To see this for $i = 1$, observe that choosing $\vec{\eta} = (\vec{z}\, \phi_k^{m,1}, 0, 0)$, $k = 1 \to \overline{K}_1$, in (3.14) yields, on assuming $\kappa_1^c \neq 0$, that for $k = 1 \to \overline{K}_1$:

$$\vec{\omega}_{1,k}^m \,.\, \vec{z} = 0 \quad \forall\ \vec{z} \in \mathbb{R}^3 \quad \Longleftrightarrow \quad \vec{\omega}_{1,k}^m = \vec{0}.$$

However, this contradicts assumption ($\mathscr{A}$) and hence $\kappa_1^c = 0$. The proof for $\kappa_2^c = 0$ is identical, and so we conclude that $\kappa_\gamma = (0,0,0)$. It now follows that

$$0 = \langle \vec{X}^c, \chi\, \vec{v}^m \rangle_m^h \equiv \langle \vec{X}^c, \chi\, \vec{\omega}^m \rangle_m^h \quad \forall\ \chi \in W^h(\Gamma^m). \tag{3.15}$$

Choosing $\chi = (\phi_k^{m,1}, 0, 0)$, $\chi = (0, \phi_k^{m,2}, 0)$ and $\chi = (0, 0, \phi_k^{m,3})$ in (3.15) yields that $\vec{X}^c \,.\, \vec{\omega}_{i,k}^m = 0$ for $k = 1 \to \overline{K}_i$, $i = 1 \to 3$. In addition, on recalling that $\vec{X} \in \underline{V}_{\vec{0}}^h(\Gamma^m)$, it holds that $\vec{X}^c \,.\, \nabla F_{d_k}(\vec{q}) = 0$ for $\vec{q} \in \widehat{\mathscr{B}}_k^m$, $k = 1 \to I_B$, and so it follows from assumption ($\mathscr{A}$) that $\vec{X}^c = \vec{0}$. Hence we have shown that there exists a unique solution $(\delta\vec{X}^{m+1}, \kappa_\gamma^{m+1}) \in \underline{V}_{\vec{0}}^h(\Gamma^m) \times W^h(\Gamma^m)$ to (3.9*a*,*b*). □

We now show that our fully discrete scheme (3.9*a*,*b*), in the absence of a tangential forcing at the external boundary, is unconditionally stable.

Theorem 3.2 *Let the assumptions* ($\mathscr{A}$) *hold, and let* $I_B = 0$ *or let* (2.19) *hold. Let* $\{(\vec{X}^m, \kappa_\gamma^m)\}_{m=1}^M$ *be the unique solution to* (3.9*a*,*b*). *Then for* $k = 1 \to M$ *we have that*

$$|\Gamma^k|_\gamma + \sum_{m=0}^{k-1} \tau_m \left\langle \kappa_\gamma^{m+1}, \kappa_\gamma^{m+1} \right\rangle_{\beta,m}^{\star,h} \leqslant |\Gamma^0|_\gamma\,. \tag{3.16}$$

https://doi.org/10.1017/S0956792510000203 Published online by Cambridge University Press

Proof Choosing $\chi = \kappa_\gamma^{m+1} \in W^h(\Gamma^m)$ in (3.9*a*) and $\vec{\eta} = \frac{\vec{X}^{m+1} - \vec{X}^m}{\tau_m} \in \underline{V}^h_{\vec{\partial}}(\Gamma^m)$ in (3.9*b*) yields that

$$\left\langle \nabla_s^{\widetilde{G}} \vec{X}^{m+1}, \nabla_s^{\widetilde{G}} (\vec{X}^{m+1} - \vec{X}^m) \right\rangle_{\gamma,m} + \tau_m \left\langle \kappa_\gamma^{m+1}, \kappa_\gamma^{m+1} \right\rangle^{\star,h}_{\beta,m} = 0. \tag{3.17}$$

It follows from [7, Lemma 3.1], similarly to the proof of Theorem 3.2 in [7], on noting that $\vec{X}^m \equiv \vec{\mathrm{id}}$ on Γ^m, that

$$\left\langle \nabla_s^{\widetilde{G}} \vec{X}^{m+1}, \nabla_s^{\widetilde{G}} (\vec{X}^{m+1} - \vec{X}^m) \right\rangle_{\gamma,m} \geqslant |\Gamma^{m+1}|_\gamma - |\Gamma^m|_\gamma. \tag{3.18}$$

Combining (3.17) and (3.18) yields that

$$|\Gamma^{m+1}|_\gamma - |\Gamma^m|_\gamma + \tau_m \left\langle \kappa_\gamma^{m+1}, \kappa_\gamma^{m+1} \right\rangle^{\star,h}_{\beta,m} \leqslant 0. \tag{3.19}$$

Summing (3.19) for $m = 0 \to k-1$ yields the desired result (3.16). □

We observe that Theorem 3.2 only applies to (3.9*a,b*) if the right-hand side in (3.9*b*) vanishes. It does not appear possibly to prove a similar stability result with a general tangential forcing term being present, i.e. a natural discrete analogue of Proposition 2.1. However, in practice we observed no restriction on the choice of time-step size even for non-zero ϱ_k. In addition, it is possible to prove such a stability result for a semi-discrete continuous in time approximation in the case of flat external boundaries (see Remark 3.2).

Remark 3.2 (Semi-discrete scheme) It is worthwhile to consider a continuous in time semi-discrete version of our scheme (3.9*a,b*). In particular, we replace (3.9*a,b*) by: Find $\vec{X} \in \underline{V}^h(\Omega^h)$ satisfying $\vec{X}_t \in \underline{V}^h_{\vec{\partial}}(\Gamma^h(t))$ and $\kappa_\gamma \in W^h(\Gamma^h(t))$ such that

$$\langle \vec{X}_t, \chi\, \vec{\nu}^h \rangle^h - \langle \kappa_\gamma, \chi \rangle^{\star,h}_\beta = 0 \quad \forall\, \chi \in W^h(\Gamma^h(t)), \tag{3.20a}$$

$$\langle \kappa_\gamma\, \vec{\nu}^h, \vec{\eta} \rangle^h + \left\langle \nabla_s^{\widetilde{G}} \vec{X}, \nabla_s^{\widetilde{G}} \vec{\chi} \right\rangle_\gamma = \sum_{k=1}^{I_B} \int_{\mathscr{B}_k^h} \varrho_k\, \vec{\xi}_k^h \cdot \vec{\eta}_{s_k}\, \mathrm{d}\mathscr{H}^1 \quad \forall\, \vec{\eta} \in \underline{V}^h_{\vec{\partial}}(\Gamma^h(t)), \tag{3.20b}$$

where we always integrate over the current surface cluster $\Gamma^h(t)$ described by the identity functions $\vec{X}(t) \in \underline{V}^h(\Gamma^h(t))$, with normals $\vec{\nu}^h(t)$, conormals $\vec{\mu}^h(t)$, triple-junction line $\mathscr{T}^h(t)$ and boundary intersection lines $\mathscr{B}_k^h(t)$. In addition, $\langle \cdot, \cdot \rangle^h$ and $\langle \cdot, \cdot \rangle^{\star,h}_\beta$ are the same as $\langle \cdot, \cdot \rangle^h_m$ and $\langle \cdot, \cdot \rangle^{\star,h}_{\beta,m}$ with Γ^m and $\vec{X}^m$ replaced by $\Gamma^h(t)$ and $\vec{X}(t)$, respectively. Similarly, $\vec{\xi}^h(t)$ is the same as (3.8), and $\underline{V}^h_{\vec{\partial}}(\Gamma^h(t))$, $W^h(\Gamma^h(t))$ are the same as (3.5*a,b*), with the obvious replacements. It is straightforward to show that (3.20*a,b*) satisfies a discrete analogue of (2.21) in the case of flat external boundaries, i.e. that

$$\frac{\mathrm{d}}{\mathrm{d}t} \left[E_\gamma(\Gamma^h) + \sum_{k=1}^{I_B} \left(\widehat{\varsigma}_k^+ |\mathscr{G}_k^{h,+}| + \widehat{\varsigma}_k^- |\mathscr{G}_k^{h,-}| \right) \right] \leqslant 0, \tag{3.21}$$

where $\overline{\mathscr{G}}_k = \overline{\mathscr{G}_k^{h,+}} \cup \overline{\mathscr{G}_k^{h,-}}$ with $\overline{\mathscr{G}_k^{h,+}} \cap \overline{\mathscr{G}_k^{h,-}} = \mathscr{B}_k^h$, such that $\vec{\xi}_k^h$ is the outer normal to $\mathscr{G}_k^{h,-}$ on $\mathscr{B}_k^h$. Note that as $\vec{\partial}\mathscr{D}_{d_k}$ is flat, it holds that $\mathscr{B}_k^h \subset \vec{\partial}\mathscr{D}_{d_k}$. In order to show (3.21), choose

https://doi.org/10.1017/S0956792510000203 Published online by Cambridge University Press

$\chi = \kappa_\gamma \in W^h(\Gamma^h(t))$ in (3.20*a*) and $\vec{\eta} = \vec{X}_t \in \underline{V}^h_{\vec{0}}(\Gamma^h(t))$ in (3.20*b*). Then using the fact that

$$\frac{\mathrm{d}}{\mathrm{d}t} E_\gamma(\Gamma^h) = \left\langle \nabla_s^{\widetilde{G}} \vec{X}, \nabla_s^{\widetilde{G}} \vec{X}_t \right\rangle_\gamma + \sum_{i=1}^{3} \int_{\partial\Gamma_i^h} \vec{X}_{i,t} \cdot \left(\gamma_i(\vec{\nu}_i^h)\, \vec{\mu}_i^h - \left(\gamma_i'(\vec{\nu}_i^h) \cdot \vec{\mu}_i^h\right) \vec{\nu}_i^h\right) \mathrm{d}\mathscr{H}^1, \quad (3.22)$$

we can argue similarly to the proof of Proposition 2.1. Here the crucial point is that the boundary integrals $\int_{\mathscr{B}_k^h} \vec{X}_{s_k,t} \cdot \vec{\xi}_k^h \, \mathrm{d}\mathscr{H}^1$ are the correct analogues of the terms appearing in (3.22), if the boundaries $\partial\mathscr{D}_{d_k}$ are flat, since then $\mathscr{B}_k^h \subset \partial\mathscr{D}_{d_k}$ form part of the true boundaries on $\partial\mathscr{D}_{d_k}$ of the enclosed areas $\mathscr{G}_k^{h,\pm}$, $k = 1 \to I_B$. In particular, the natural finite-element analogue of (2.23) will still hold in the case of flat boundaries, but does not hold in general.

Remark 3.3 (More complicated surface cluster set-ups) Throughout this paper, for simplicity, we restrict ourselves to surface cluster set-ups involving exactly three surfaces, i.e. two material surfaces and one grain boundary, meeting at a single triple-junction line; and this will be sufficient for the majority of the numerical experiments presented in Section 6. However, using the techniques developed in [8], where variational formulations and fully practical finite-element approximations for the (anisotropic) mean curvature flow, recall (2.2) for the isotropic case, and for the (anisotropic) surface diffusion, recall (2.3) for the isotropic case, of arbitrary types of surface clusters were introduced, it is not difficult to generalise our approximation (3.9*a,b*) for (2.36*a,b*) to more complicated surface clusters. In general, there will be $I_S \geqslant 3$ surfaces meeting at $I_T \geqslant 1$ triple-junction lines, with the possibility of four triple-junction lines meeting at quadruple junction points. Then the weak formulation (2.36*a,b*) will still be valid on generalising the inner products and trial and test spaces in the obvious fashion. Repeating this process on the discrete level then yields the natural generalisations of (3.9*a,b*) to these more general situations. Although we do not state the details for our approximation in these cases – the interested reader is referred to [8] for the necessary notation – we do present some computations in Section 6.

In addition, it is not difficult to generalise our approximation to models with junction lines, where more than three surfaces meet. However, as such higher-order junction lines, such as quadruple junction lines, are in general unstable and hence of little practical interest, we restrict ourselves to triple-junction lines in this paper.

Remark 3.4 (The two-dimensional case) The scheme (3.9*a,b*) is the natural extension to surface clusters and anisotropic surface energies of the finite-element approximation for the isotropic evolution of curve networks in the plane considered in [2, (2.53*a,b*)]. In fact, it is a simple matter to combine the scheme in [2] for the flow (2.4) in the plane with the techniques for anisotropic surface energies for curve networks in [4] in order to derive an, in general, unconditionally stable parametric finite-element approximation of (2.14) in the plane, i.e. the two-dimensional analogue of (3.9*a,b*). Apart from the obvious changes in the definitions of the inner products and test and trial spaces, the two-dimensional and three-dimensional versions of our scheme differ slightly in how the condition (2.18*a*) may be handled. Clearly, in the two-dimensional case, the weak formulation of these boundary conditions gives rise to the term $\sum_{k=1}^{I_B} \varrho_k \, (\vec{\xi}_k \cdot \vec{\eta}_{s_k}) \, |_{\mathscr{B}_k}$ on the right-hand side of (2.36*b*),

https://doi.org/10.1017/S0956792510000203 Published online by Cambridge University Press

where the vectors $\vec{\xi}_k$, defined by (2.20), are tangential to $\partial\mathscr{D}_{d_k}$. Hence $\vec{\xi}_k$ can also be written in terms of $\vec{n}_{d_k}^{\perp}$, where $\cdot^{\perp}$ denotes the clockwise rotation by 90° in $\mathbb{R}^2$. In particular, we have that $\vec{\xi}_k = o_k\,\vec{n}_{d_k}^{\perp}$, where $o_k := ([\frac{\partial}{\partial s}\,\vec{x}_{s_k}]\,.\,\vec{\mu}_{s_k})|_{\mathscr{B}_k}$ defines a correction factor $o_k \in \{-1, 1\}$, which ensures that $(\vec{n}_{d_k}, \vec{\xi}_k)$ have the same orientation as $(\vec{\nu}_{s_k}, \vec{\mu}_{s_k})$, analogously to the three-dimensional case; recall (2.20). We note that in our previous papers on the two-dimensional case, for simplicity, we always assumed that $\frac{\partial}{\partial s}\,\vec{x}_{s_k} = \vec{\mu}_{s_k}$ at $\mathscr{B}_k$, so that $o_k = 1$ and $\vec{\xi}_k = \vec{n}_{d_k}^{\perp}$; see [2, 4]. On the discrete level, the vectors $\vec{\xi}_k$ are approximated by $\vec{\xi}_k^{\,m} = o_k\,\frac{[\nabla F_{d_k}(\mathscr{B}_k^m)]^{\perp}}{|\nabla F_{d_k}(\mathscr{B}_k^m)|}$, $k = 1 \to I_B$, which yields the natural two-dimensional analogue of the right-hand side in (3.9*b*); see also [4, (2.38)]. The fact that our approximations for the two and three-dimensional case are so similar is the motivation for including some two-dimensional numerical experiments based on this scheme in Section 5, in particular as such results for anisotropic surface energies have not yet been published by the authors.

Finally, we remark that it is not difficult to show that in the two-dimensional case, the semi-discrete scheme (3.20*a,b*) satisfies the energy bound (3.21) even for curved external boundaries. That is because here the boundary intersections $\mathscr{B}_k^h$ reduce to points on the boundary $\partial\mathscr{D}_{d_k}$, and so it holds that $\mathscr{B}_k^h \in \partial\mathscr{D}_{d_k}$ at all times. In addition, it is possible to prove stability for the fully discrete scheme in the case of flat boundaries, something that in general does not hold in the three-dimensional situation. This again relies on the fact that now $\mathscr{B}_k^m \in \partial\mathscr{D}_{d_k}$ for all $m = 1 \to M$, $k = 1 \to I_B$; and it is not difficult to show that

$$|\Gamma^{m+1}|_\gamma + \sum_{k=1}^{I_B} \left(\widehat{\varsigma}_k^{+}\,|\mathscr{G}_k^{m+1,+}| + \widehat{\varsigma}_k^{-}\,|\mathscr{G}_k^{m+1,-}|\right) \leqslant |\Gamma^{m}|_\gamma + \sum_{k=1}^{I_B} \left(\widehat{\varsigma}_k^{+}\,|\mathscr{G}_k^{m,+}| + \widehat{\varsigma}_k^{-}\,|\mathscr{G}_k^{m,-}|\right), \quad (3.23)$$

for all $m = 0 \to M-1$; where $\mathscr{G}_k^{m+1,\pm}$ are straight lines segments on $\partial\mathscr{D}_{d_k}$. The proof of (3.23) proceeds as the proof of Theorem 3.2. In particular, choosing $\chi = \kappa_\gamma^{m+1} \in W^h(\Gamma^m)$ and $\vec{\eta} = \frac{\vec{X}^{m+1} - \vec{X}^m}{\tau_m} \in \underline{V}_\partial^h(\Gamma^m)$ in the two-dimensional analogues of (3.9*a,b*) yields that

$$|\Gamma^{m+1}|_\gamma - |\Gamma^{m}|_\gamma - \sum_{k=1}^{I_B} \varrho_k \left(\mathscr{B}_k^{m+1} - \mathscr{B}_k^{m}\right).\vec{\xi}_k \leqslant 0,$$

on noting that $\vec{\xi}_k^{\,m+1} = \vec{\xi}_k^{\,m} = \vec{\xi}_k$ for all $k = 1 \to I_B$. Observing that $\varrho_k\,(\mathscr{B}_k^{m+1} - \mathscr{B}_k^{m}).\vec{\xi}_k = (\widehat{\varsigma}_k^{+}\,|\mathscr{G}_k^{m,+}| + \widehat{\varsigma}_k^{-}\,|\mathscr{G}_k^{m,-}|) - (\widehat{\varsigma}_k^{+}\,|\mathscr{G}_k^{m+1,+}| + \widehat{\varsigma}_k^{-}\,|\mathscr{G}_k^{m+1,-}|)$ then yields the desired result (3.23).

4 Solution of the discrete systems

In this section, we introduce a computationally convenient equivalent reformulation of our scheme (3.9*a,b*). It is an extension of an approach introduced in [8] for schemes approximating the flows (2.2) and (2.3), and their anisotropic equivalents, for very general types of clusters.

Let $K := \sum_{i=1}^{3} K_i$ and, for later reference, let $J := \sum_{i=1}^{3} J_i$. In addition, let $\vec{Id} \in \mathbb{R}^{3\times 3}$ be the identity matrix. We define the orthogonal projection $\vec{\mathscr{P}}_\partial : (\mathbb{R}^3)^K \to \underline{\mathbb{X}}_\partial$ onto the Euclidean space associated with $\underline{V}_\partial^h(\Gamma^m)$, and similarly $\mathscr{K} : \mathbb{R}^K \to \mathbb{X}$ the orthogonal projection onto the Euclidean space associated with $W^h(\Gamma^m)$. The two projections $\mathscr{K}$ and

https://doi.org/10.1017/S0956792510000203 Published online by Cambridge University Press

$\vec{\mathscr{P}}_\partial$ are crucial in the construction of fully practical solution methods for the finite-element approximations introduced in Section 3. With the help of these two projections it will be sufficient throughout to work with the bases of the simple product finite-element spaces $\widehat{W}^h(\Gamma^m)$ and $\underline{\widehat{V}}^h(\Gamma^m)$, recall (3.4), rather than having to work with the highly non-trivial trial and test spaces $W^h(\Gamma^m)$ and $\underline{V}^h_\partial(\Gamma^m)$ directly. For more details we refer to [8].

In order to give a matrix formulation for (3.9*a,b*), we introduce the matrices $M^i_\beta, A^i_\beta \in \mathbb{R}^{K_i\times K_i}$, $\vec{N}^i \in (\mathbb{R}^3)^{K_i\times K_i}$ and $\vec{A}^i, \vec{A}^i_\gamma \in (\mathbb{R}^{3\times 3})^{K_i\times K_i}$, $i = 1 \to 3$, defined by

$$
\begin{aligned}
\big[M^i_\beta\big]_{kl} &:= \int_{\Gamma^m_i} \beta_i\big(\vec{v}^m_i\big)\, \pi^m_i\big[\phi^{m,i}_k\, \phi^{m,i}_l\big]\, \mathrm{d}\mathscr{H}^2, \quad \vec{N}^i_{kl} := \int_{\Gamma^m_i} \pi^m_i\big[\phi^{m,i}_k\, \phi^{m,i}_l\big]\, \vec{v}^m_i\, \mathrm{d}\mathscr{H}^2,\\
\big[A^i_\beta\big]_{kl} &:= \int_{\Gamma^m_i} \beta_i\big(\vec{v}^m_i\big)\, \nabla_s\, \phi^{m,i}_k \,.\, \nabla_s\, \phi^{m,i}_l\, \mathrm{d}\mathscr{H}^2, \quad \vec{A}^i_{kl} := \left(\int_{\Gamma^m_i} \nabla_s\, \phi^{m,i}_k \,.\, \nabla_s\, \phi^{m,i}_l\, \mathrm{d}\mathscr{H}^2\right) \vec{Id}, \qquad (4.1)\\
\big[\vec{A}^i_\gamma\big]_{kl} &:= \left(\left\langle \nabla^{\widetilde{G}_i}_s\, \big(\phi^{m,i}_k\, \vec{\mathrm{e}}_n\big), \nabla^{\widetilde{G}_i}_s\, \big(\phi^{m,i}_l\, \vec{\mathrm{e}}_j\big)\right\rangle_{\gamma_i,m,i}\right)^3_{n,j=1},
\end{aligned}
$$

where $\{\vec{\mathrm{e}}_i\}^3_{i=1}$ denotes the standard basis in $\mathbb{R}^3$, and where we recall (3.7). In addition, we recall that $\{\{\phi^{m,i}_k\}^{K_i}_{k=1}\}^3_{i=1}$ is the standard basis of $\widehat{W}^h(\Gamma^m)$ and $\pi^m := (\pi^m_1, \pi^m_2, \pi^m_3) : C(\Gamma^m, \mathbb{R}) \to \widehat{W}^h(\Gamma^m)$ is the standard interpolation operator at the nodes $\{\{\vec{q}^{\,m,i}_k\}^{K_i}_{k=1}\}^3_{i=1}$. The assembly of matrices as they appear in (4.1) is by now standard in the finite-element literature (see e.g. [20, 21, 23]). Only the matrices $\vec{A}^i_\gamma$ are an exception due to the non-standard differential operators that are involved. However, also their assembly is straightforward and further details on their assembly can be found in e.g. [7, Section 4].

Then, on introducing the matrices

$$
B := \mathrm{diag}\,\big(A^1_\beta, A^2_\beta, M^3_\beta\big), \quad \vec{A}_\gamma := \mathrm{diag}(\vec{A}^1_\gamma, \vec{A}^2_\gamma, \vec{A}^3_\gamma), \quad \vec{N} := \mathrm{diag}(\vec{N}^1, \vec{N}^2, \vec{N}^3),
$$

where $B : \mathbb{R}^K \to \mathbb{R}^K$, $\vec{A}_\gamma : (\mathbb{R}^3)^K \to (\mathbb{R}^3)^K$ and $\vec{N} : \mathbb{R}^K \to (\mathbb{R}^3)^K$, the system of equations (3.9*a,b*) can be equivalently written as: Find $(\delta\vec{X}^{m+1}, \kappa^{m+1}_\gamma) \in \underline{\mathbb{X}}_\partial \times \mathbb{X}$ such that

$$
\begin{pmatrix} \mathscr{K} B \mathscr{K} & -\frac{1}{\tau_m}\, \mathscr{K} \vec{N}^T \vec{\mathscr{P}}_\partial \\ \vec{\mathscr{P}}_\partial \vec{N} \mathscr{K} & \vec{\mathscr{P}}_\partial \vec{A}_\gamma \vec{\mathscr{P}}_\partial \end{pmatrix} \begin{pmatrix} \kappa^{m+1}_\gamma \\ \delta\vec{X}^{m+1} \end{pmatrix} = \begin{pmatrix} 0 \\ \vec{\mathscr{P}}_\partial [\vec{f} - \vec{A}_\gamma\, \vec{X}^m] \end{pmatrix}, \qquad (4.2)
$$

where $\vec{f} = (\vec{f}^1, \vec{f}^2, \vec{f}^3)$ with $\vec{f}^i \in (\mathbb{R}^3)^{K_i}$, $i = 1 \to 3$, defined by

$$
\vec{f}^i_l = \sum_{k\in\{j=1\to I_B\,:\, s_j=i\}} \int_{\mathscr{B}^m_k} \varrho_k\, \phi^{m,i}_l\, \vec{\xi}^m_k\, \mathrm{d}\mathscr{H}^1, \quad l = 1 \to K_i.
$$

Here, with the obvious abuse of notation, $\kappa^{m+1}_\gamma \in \mathbb{R}^K$ and $\delta\vec{X}^{m+1} \in (\mathbb{R}^3)^K$ are the vectors of coefficients with respect to the standard basis $\{\{\phi^{m,i}_k\}^{K_i}_{k=1}\}^3_{i=1}$ of κ^{m+1}_γ and $\vec{X}^{m+1} - \vec{X}^m$ in (3.9*a,b*), respectively.

Remark 4.1 (The isotropic case) On recalling Remark 3.1, we note that the linear system of equations needing to be solved at each time level for the approximation (3.11*a,b*), for the simpler case of isotropic surface energy densities (2.12), is equivalent to: Find

https://doi.org/10.1017/S0956792510000203 Published online by Cambridge University Press

$(\delta\vec{X}^{m+1}, \kappa^{m+1}) \in \underline{\mathbb{X}}_\partial \times \mathbb{R}^K$ such that $\kappa_i^{m+1} = \varsigma_i^{-1}\,\kappa_{\gamma,i}^{m+1}$, $i = 1 \to 3$, where $(\delta\vec{X}^{m+1}, \kappa_\gamma^{m+1}) \in \underline{\mathbb{X}}_\partial \times \mathbb{X}$ are the solution of

$$\begin{pmatrix} \mathcal{K}B\mathcal{K} & -\frac{1}{\tau_m}\,\mathcal{K}\vec{N}^T\vec{\mathcal{P}}_\partial \\ \vec{\mathcal{P}}_\partial\vec{N}\mathcal{K} & \vec{\mathcal{P}}_\partial\vec{A}_\varsigma\vec{\mathcal{P}}_\partial \end{pmatrix} \begin{pmatrix} \kappa_\gamma^{m+1} \\ \delta\vec{X}^{m+1} \end{pmatrix} = \begin{pmatrix} 0 \\ \vec{\mathcal{P}}_\partial[\vec{f} - \vec{A}_\varsigma\,\vec{X}^m] \end{pmatrix},$$

with $\vec{A}_\varsigma := \mathrm{diag}(\varsigma_1\vec{A}^1, \varsigma_2\vec{A}^2, \varsigma_3\vec{A}^3)$. Hence for the solution of (3.11*a,b*) only the standard finite-element matrices occurring in (4.1) are needed.

Hence computing solutions to our approximation (3.9*a,b*) reduces to solving the linear system (4.2). In practice it is convenient to solve (4.2) with the help of a Schur complement approach, which reduces (4.2) to a symmetric, positive semi-definite system. We now derive this Schur complement (see also [8] for a similar approach).

On noting that $\mathcal{K}B\mathcal{K}$ is a symmetric, positive semi-definite matrix, we first introduce the inverse S of $\mathcal{K}B\mathcal{K}$ on the space $(\ker\mathcal{K}B\mathcal{K})^\perp$, where $\cdot^\perp$ acting on a space denotes its orthogonal complement. That is, S is the unique linear operator such that $S\,\mathcal{K}B\mathcal{K}\,v = \mathcal{K}B\mathcal{K}\,S\,v = v$ for all $v \in (\ker\mathcal{K}B\mathcal{K})^\perp$. In addition, let $\vec{\Pi} : (\mathbb{R}^3)^K \to \mathcal{R}^\perp$ be the orthogonal projection onto $\mathcal{R}^\perp$, where $\mathcal{R} := \mathrm{span}\{\vec{\mathcal{P}}_\partial\vec{N}\mathcal{K}\,e_1\} \equiv \{\vec{\mathcal{P}}_\partial\vec{N}\mathcal{K}\,v : v \in \ker\mathcal{K}B\mathcal{K}\} \subset \underline{\mathbb{X}}_\partial$, with $e_1 = (\underline{1}^1, -\underline{1}^2, \underline{0}^3)^T$ being a spanning vector of the space $\ker\mathcal{K}B\mathcal{K} \equiv \ker B \cap \mathbb{X}$, where $\underline{1}^i = (1, \ldots, 1) \in \mathbb{R}^{K_i}$ and similarly for $\underline{0}^i$, $i = 1 \to 3$. Then the solution $\delta\vec{X}^{m+1} \in \underline{\mathbb{X}}_\partial$ of (4.2) can be found by applying a Schur complement approach and then solving

$$\vec{\Pi}\,\vec{\mathcal{P}}_\partial\big(\vec{A}_\gamma + \tfrac{1}{\tau_m}\,\vec{N}\mathcal{K}\,S\,\mathcal{K}\vec{N}^T\big)\,\vec{\mathcal{P}}_\partial\;\vec{\Pi}\,\delta\vec{X}^{m+1} = \vec{\Pi}\,\vec{\mathcal{P}}_\partial[\vec{f} - \vec{A}_\gamma\,\vec{X}^m]. \tag{4.3}$$

The Schur complement system (4.3) can be solved with a (preconditioned) conjugate gradient solver. Here we used a simple diagonal preconditioner as considered in [4, p. 314] for the two-dimensional case. The solution of $\mathcal{K}B\mathcal{K}\,y = x$ in order to compute $S\,x$ can be obtained with an (inner loop) conjugate gradient (CG) solver without a projection, as the right-hand side vector x always satisfies the necessary compatibility condition, i.e. $x \in (\ker\mathcal{K}B\mathcal{K})^\perp$. See [29] for a justification of using a CG solver for a positive semi-definite system.

5 Numerical results in two dimensions

On recalling Remark 3.4, we now present some numerical simulations for a simplified two-dimensional model of coupled surface and grain boundary motion. Here we utilise the finite-element approximations developed in [2, 4], which lead to the precise two-dimensional analogue of (3.9*a,b*), i.e. a scheme for coupled anisotropic surface diffusion and anisotropic curvature flow in the plane.

Throughout this section, for simplicity, we will often not number each curve making up the curve network individually. Instead, we will at times prescribe e.g. surface energy densities ς_i, or mobilities β_i, for curves Γ_i collectively with the help of parameters ς_s and ς_{gb}, in cases were these are the same for all curves representing material surfaces and grain boundaries, respectively. Here we recall that material surfaces are modelled by

https://doi.org/10.1017/S0956792510000203 Published online by Cambridge University Press

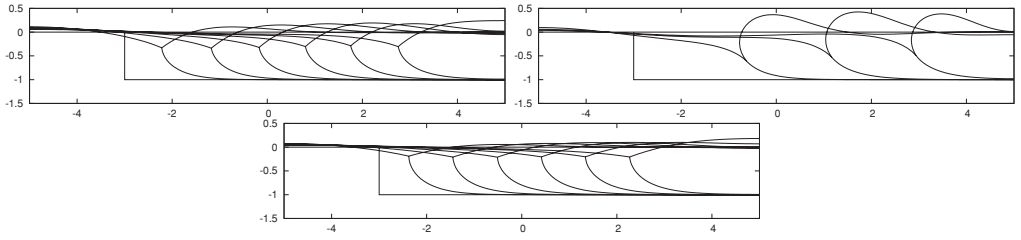

FIGURE 2. Travelling wave solutions at times $t = 0, 0.5, \ldots, T$, with $T = 3,\ 1.5,\ 3$, for $\varsigma = (1,1,1)$, $\varsigma = (1,1,2)$ and $\varsigma = (2,2,1)$.

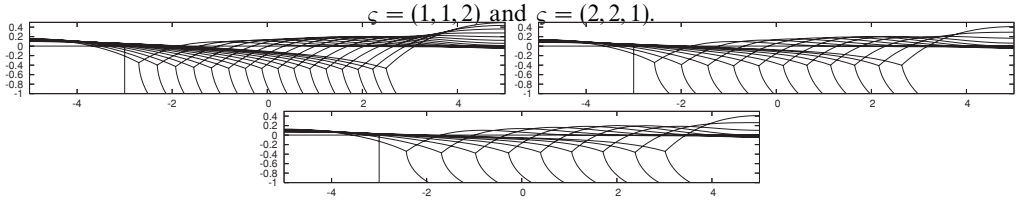

FIGURE 3. Travelling wave solutions at times $t = 0, 0.5, \ldots, T$, with $T = 8,\ 5.5,\ 4.4$, for the contact angles $\alpha = 60^\circ,\ 45^\circ,\ 30^\circ$.

curves moving by surface diffusion, while grain boundaries are modelled by curves that move by mean curvature flow.

Finally, we use uniform time steps $\tau_m = \tau$, $m = 0 \to M-1$, and usually state the external domain $\mathscr{D}$, rather than its parts $\partial\mathscr{D}_j$, $j = 1 \to I_D$, throughout this section.

5.1 Isotropic flows

In this section, we consider the isotropic case (2.12). Unless otherwise stated, we assume that $\varsigma = (1,1,1)$, $\beta = (1,1,1)$ and that (2.19) holds.

We start with a so called quarter loop design as presented in [2, Figure 28], and note that the scheme mentioned in Remark 3.4 for the isotropic situation considered here corresponds precisely to the approximation introduced in that paper. The computations shown in Figure 2 start with three curves meeting at a single triple-junction point, of which the two horizontal ones experience motion by surface diffusion, while the third curve undergoes motion by mean curvature. As surface energies we choose $\varsigma = (1,1,1)$, $\varsigma = (1,1,2)$ or $\varsigma = (2,2,1)$. The external domain is $\mathscr{D} = (-5,5) \times \mathbb{R}$ and we have $I_B = 3$. The chosen discretisation parameters are $K = 258$, $J = 255$ and $\tau = 10^{-3}$. We observe that the evolutions in Figure 2 exhibit travelling wave solutions, where the profile of the travelling wave is highly dependent on the chosen surface energies ς. Such travelling wave solutions were first mentioned in [37] (see also [31,32]).

Similar travelling wave solutions can be observed for a slightly simpler set-up, where the initial curves form a letter 'T', but where at the external boundary a non-90° angle condition is prescribed for the grain boundary Γ_3. Numerical simulations for such a situation have been performed in e.g. [44,45]. We present such numerical results for our finite-element approximation in Figure 3, where the external domain is given by $\mathscr{D} = (-5,5) \times (-1,\infty)$ and $I_B = 3$. The discretisation parameters are $K = 129$, $J = 126$ and $\tau = 10^{-3}$. We choose $\varsigma = (1,1,1)$ and $\varrho_3 = \cos\alpha$, with $\alpha = 60^\circ, 45^\circ, 30^\circ$, where ϱ_3

https://doi.org/10.1017/S0956792510000203 Published online by Cambridge University Press

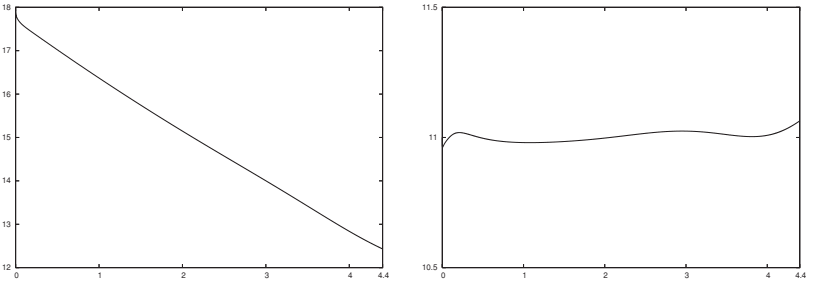

FIGURE 4. Plots of $\widetilde{\mathscr{E}}(\Gamma^m)$ and $|\Gamma^m|$ over time.

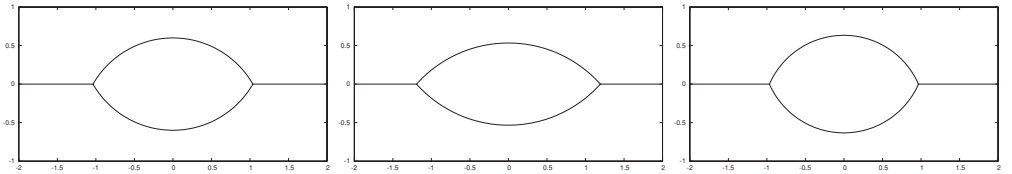

FIGURE 5. Numerical steady states for $\varsigma_{gb} = 1$ and $\varsigma_s = 1, \frac{3}{4}, \frac{5}{4}$.

denotes the difference in boundary contact energy densities to the right and to the left of Γ_3. This choice of ϱ_3 will enforce a contact angle of α at the lower boundary for the curve Γ_3. As is to be expected, we note from the numerical results in Figure 3 that the smaller the contact angle, the faster the travelling wave moves through the domain from left to right. On recalling (3.23), for the case $\alpha = 30^\circ$ we also present a plot of the discrete energy

$$\widetilde{\mathscr{E}}(\Gamma^m) := |\Gamma^m| + \sum_{k=1}^{I_B} \varrho_k \left|\mathscr{G}_k^{m,+}\right|$$

over time in Figure 4. As a comparison, we also show the evolution of the surface area of Γ^m, where we note that $\widetilde{\mathscr{E}}(\Gamma^0) - |\Gamma^0| = 8\,\varrho_3 = 8\cos 30^\circ \approx 6.93$, and so very different scales are used for the two plots. As was shown in Remark 3.4, the total energy $\widetilde{\mathscr{E}}(\Gamma^m)$ decreases monotonically in time, whereas the surface area of Γ^m alone does not.

The next experiments are for a simplified two-dimensional model of a trapped volume of air between two different grains of the same material. Hence the curve network consists of $I_S = 4$ curves with $I_T = 2$ triple-junction points and $I_B = 2$ boundary intersection points. In Figure 5 we present the numerical steady-state solutions for this set-up for different values of the (isotropic) energy densities ς_{gb} and ς_s for grain boundaries and material surfaces, respectively. The external domain is $\mathscr{D} = (-2, 2) \times \mathbb{R}$ and the discretisation parameters are $K = 258$, $J = 254$, $\tau = 10^{-3}$ and $T = 1$. Similar to Figure 3, travelling wave solutions can be obtained by enforcing a non-90° contact angle at the external boundaries. For instance, repeating the experiment in Figure 5 for $\varsigma = (1, 1, 1)$ and choosing $\varrho_1 = \varrho_2 = \cos\alpha$, with $\alpha = 60^\circ, 45^\circ, 30^\circ$, for the tangential forcing at the left and right boundary, leads to the void and the grain boundary travelling with a constant velocity through the material. Here ϱ_k denotes the difference in boundary contact energies

https://doi.org/10.1017/S0956792510000203 Published online by Cambridge University Press

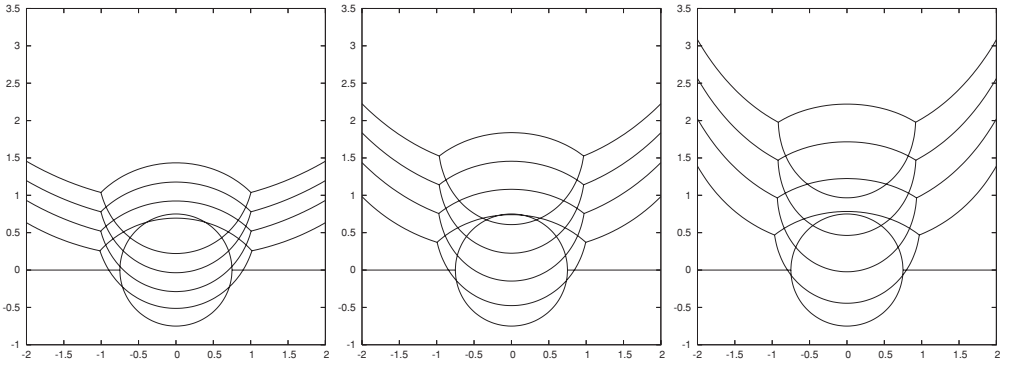

FIGURE 6. Travelling wave solutions at times $t = 0, 1, \ldots, 4$ for the contact angles $\alpha = 60°, 45°, 30°$.

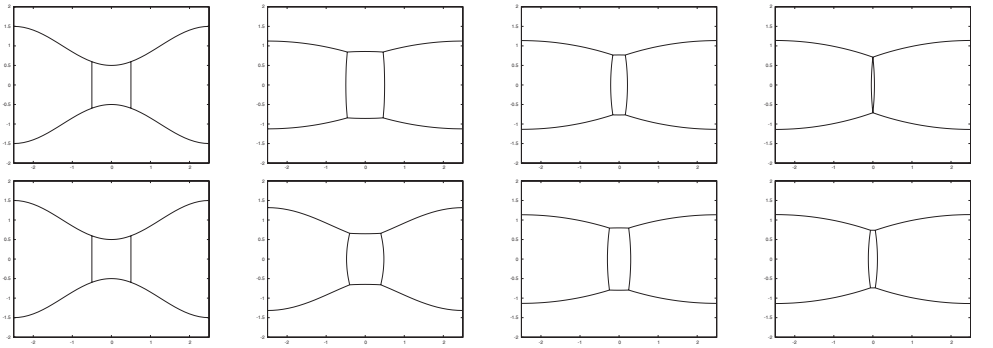

FIGURE 7. Sintering simulation at times $t = 0, 0.1, 2, 2.9$ for $\beta_s = 100$. Below the solution at times $t = 0, 0.1, 1, 2$ for $\beta_s = 1$.

above and below Γ_{s_k}, $k = 1 \to 2$. The observed profiles in Figure 6 are not dissimilar to shapes known from intergranular void electromigration (see e.g. [3]).

Finally, we present a simulation for a simplified two-dimensional model of sintering, as considered in e.g. [16, Figure 7]. The set-up consists of a tubular material with three grains (see Figure 7); and the curve network consists of $I_S = 8$ curves with $I_T = 4$ triple-junction points and $I_B = 4$ boundary intersection points. The surface boundaries are attached to the external domain $\mathscr{D} = (-\frac{5}{2}, \frac{5}{2}) \times \mathbb{R}$ and initially they can be parameterised via $(z, \pm[1 - \frac{1}{2}\cos(\frac{2\pi z}{5})])$ for $z \in [-\frac{5}{2}, \frac{5}{2}]$. The two vertical grain boundaries are located at $x_1 = \pm\frac{1}{2}$. The ratio between surface energy and grain boundary energy is chosen as $\varsigma_s/\varsigma_{gb} = 3/1 = 3$, and we vary the mobility β_s, while $\beta_{gb} = 1$. The discretisation parameters are $K = 136$, $J = 128$, $\tau = 10^{-3}$. The results are shown in Figure 7, where we observe that the middle grain initially grows in size for large values of the mobility β_s, and for large mobilities only. A similar qualitative behaviour was reported in [16].

5.2 Anisotropic flows

In this subsection, we present some computations for the two-dimensional analogue of the scheme (3.9*a,b*), which is easily obtained on combining the techniques presented in [2,4];

https://doi.org/10.1017/S0956792510000203 Published online by Cambridge University Press

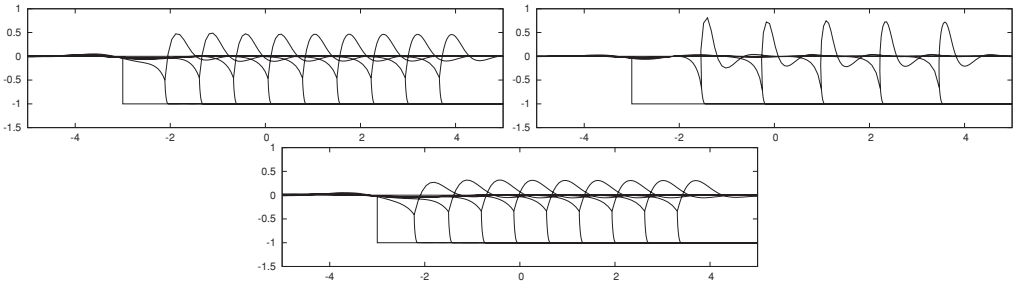

FIGURE 8. Anisotropic travelling wave solutions at times $t = 0, 0.5, \ldots, T$, with $T = 4.5$, 2.5, 4.5, for $\varsigma = (1,1,1)$, $\varsigma = (1,1,2)$ and $\varsigma = (2,2,1)$.

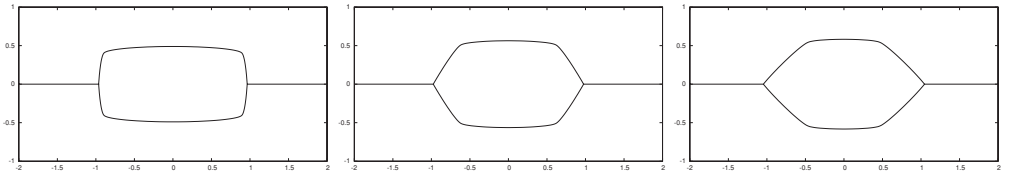

FIGURE 9. Numerical steady states for different anisotropies.

recall Remark 3.4. Unless otherwise stated, we let $\beta = (1,1,1)$ and assume that (2.19) holds.

In a first experiment we choose $\gamma = (\varsigma_1 \gamma_0, \varsigma_2 \gamma_0, \varsigma_3 \gamma_0)$ with $\gamma_0(\vec{p}) = [p_1^2 + \varepsilon^2 p_2^2]^{\frac{1}{2}}$, where $\varepsilon = 0.1$, and repeat the experiments in Figure 2. As can be seen in Figure 8, the observed travelling wave profile exhibits a much sharper front compared to the results in Figure 2. In fact, the pronounced pits in the material are not dissimilar to the three-dimensional atomic force microscope (AFM) images shown in [52, Figure 3].

In the next experiment we provide anisotropic versions of the numerical steady states shown in Figure 5. In particular, we choose $\gamma = (\gamma_1, \gamma_1, \gamma_1)$ with $\gamma_1(\vec{p})$ defined as in [4, (1.6)] with $L = 2, 3, 4$ and $\varepsilon = 0.1$, so that they correspond to the first three anisotropies displayed in [4, Figure 1]. The numerical results, for the same discretisation parameters as in Figure 5, can be seen in Figure 9, where we observe the strong influence of the chosen respective anisotropy.

6 Numerical results in three dimensions

In this section, we present several numerical simulations of evolving surface clusters in $\mathbb{R}^3$. We stress that all of the presented experiments were performed without any remeshing. In fact, in practice the initial mesh quality is maintained or even improved on by the intrinsically induced tangential motion of our schemes. A more detailed discussion of this property in the single closed hypersurface case can be found in [6], while excellent mesh properties for fully anisotropic surface energies in the closed surface case have been demonstrated in numerical experiments in [7, Section 5].

We implemented our approximation (3.9*a,b*) within the finite-element toolbox ALBERTA (see [43]), and used uniform time steps $\tau_m = \tau$, $m = 0 \to M - 1$, throughout. For

https://doi.org/10.1017/S0956792510000203 Published online by Cambridge University Press

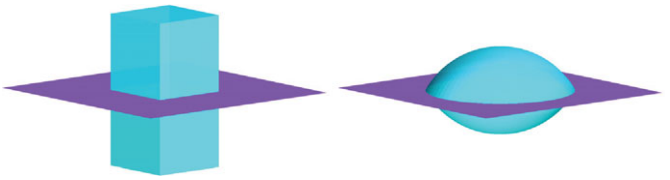

FIGURE 10. (Colour online) Initial set-up and numerically steady-state solution for equal surface energies.

the illustrations in this section we will usually not display the external boundaries $\partial\mathscr{D}_j$, $j = 1 \to I_D$, and when describing the experimental set-up we will in general only state $\mathscr{D}$, recall (2.7), rather than all $\mathscr{D}_j$, $j = 1 \to I_D$. Moreover, the grain boundaries, e.g. Γ_3 in the standard set-up (2.14) for $I_S = 3$, will be coloured in a shade of purple, while the material interfaces, e.g. Γ_1 and Γ_2 in the standard set-up, are coloured in cyan.

As in Section 5, for simplicity, we will at times use the notation e.g. ς_s and ς_{gb}, in order to collectively refer to the surface energy densities of the surfaces representing material surfaces and grain boundaries, respectively.

6.1 Isotropic flows

Firstly, we present numerical simulations for isotropic surface energy densities, (2.12), so that the free energy (2.10) reduces to

$$E_\gamma(\Gamma) = \sum_{i=1}^{3} \varsigma_i \, |\Gamma_i| \,. \tag{6.1}$$

For the presented computations we employ the scheme (3.9*a*,*b*), where we recall that for the energy (6.1) this scheme is equivalent to the approximation (3.11*a*,*b*). Unless otherwise stated, we set $\varsigma = (1,1,1)$, $\beta \equiv (1,1,1)$ and assume that (2.19) holds.

The first experiments are for a trapped volume of air between two different grains of the same material, i.e. the full three-dimensional analogue of the situation considered in e.g. Figure 5. Here we choose the initial shape of the air bubble to be a cuboid of dimensions $1 \times 1 \times 2$, with the grain boundary $\Gamma_3^0 = ([-\frac{3}{2},\frac{3}{2}]^2 \setminus (-\frac{1}{2},\frac{1}{2})^2) \times \{0\}$ being attached to the outer boundary of $\mathscr{D} = (-\frac{3}{2},\frac{3}{2})^2 \times \mathbb{R}$, recall (2.7), so that $I_B = 4$. Under the prescribed flow (2.38), the surface cluster finds a steady state that satisfies the expected contact angle conditions, i.e. 120° at the triple junction and 90° at the external boundary. The discretisation parameters are $K = 2814$, $J = 5420$, $\tau = 10^{-3}$ and $T = 0.5$. See Figure 10 for the results. We also investigated different steady-state solutions depending on the chosen surface energy densities ς in (6.1). First we used the values $\varsigma = (\varsigma_s, \varsigma_s, 1)$ with $\varsigma_s = \frac{3}{4}$ or $\varsigma_s = \frac{5}{4}$, so that the true triple-junction dihedral angle, which satisfies

$$\theta_3 = 2 \arccos(\tfrac{1}{2\varsigma_s}), \tag{6.2}$$

recall (2.17), is either $\theta_3 = 96°$ or 133°. See Figure 11 for the results, where, in addition, we also show the numerical steady-state solution for the surface energy densities $\varsigma = (\frac{5}{4},\frac{3}{4},1)$.

https://doi.org/10.1017/S0956792510000203 Published online by Cambridge University Press

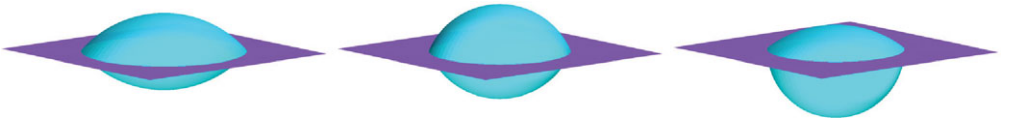

FIGURE 11. (Colour online) Numerical steady-state solutions for $\varsigma = (\frac{3}{4}, \frac{3}{4}, 1)$ and $\varsigma = (\frac{5}{4}, \frac{5}{4}, 1)$. On the right the solution for $\varsigma = (\frac{5}{4}, \frac{3}{4}, 1)$.

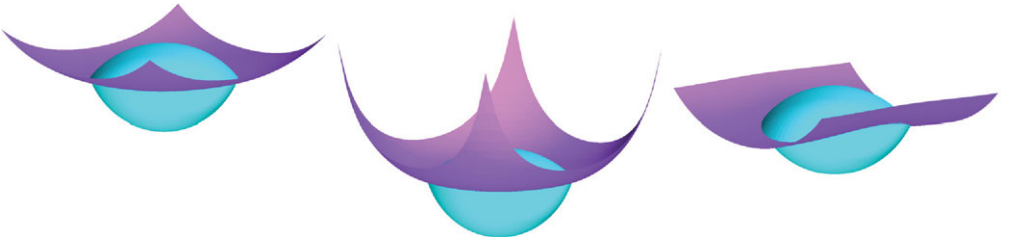

FIGURE 12. (Colour online) Profile of travelling wave solution at time $T = 0.5$. Prescribed contact angles are $\alpha = 60^\circ$ and $\alpha = 45^\circ$ (globally), as well as $\alpha = 45^\circ$ on left/right with $\alpha = 90^\circ$ at front/back.

In addition, and similarly to Figure 6, we also study the effect of enforcing a non-90° contact angle at the external boundary. As is to be expected, in this case we observe the natural three-dimensional analogues of the travelling wave solutions considered earlier. Starting with the same initial data as in Figure 10 and using the discretisation parameters $K = 4802$, $J = 9216$, $\tau = 10^{-3}$, $T = 0.5$, we plot the solutions Γ^M for the surface energies $\varsigma = (1, 1, 1)$ and the tangential forcing $\varrho_k = \cos\alpha$, $k = 1 \to 4$, with $\alpha = 60^\circ$ and $\alpha = 45^\circ$, in Figure 12. Here ϱ_k, $k = 1 \to 4$, denote the difference in the contact energy with the external boundary above and below Γ_3. For smaller angles, e.g. $\alpha = 30^\circ$, the four corners of the grain boundary become almost singular and grow towards infinity, and so we omitted these results. Similar singularity formations and a resulting discontinuous dependence on the contact angle is known in the theory of equilibrium capillary surfaces (see [24, Chapter 6] and [17]). In addition we show the profile of the travelling wave solution for the choice $\varrho_1 = \varrho_3 = 2^{-\frac{1}{2}}$ and $\varrho_2 = \varrho_4 = 0$, which corresponds to enforcing a contact angle of $\alpha = 45^\circ$ on the left and right boundary, while a standard 90° contact angle is prescribed on the remaining external boundary.

A similar set-up to Figure 10, but instead considering the two upper surfaces as material boundaries with the lower surface representing a grain boundary, was studied in the radially symmetric case in [34]. We present a numerical computation in Figure 13, where we observe that the smaller grain quickly shrinks to a point. Moreover, we note that the solution appears to attain a radially symmetric profile within a short amount of time. The discretisation parameters for this simulation are $K = 3778$, $J = 7168$, $\tau = 10^{-3}$ and $T = 0.1$, with the external domain given by $\mathscr{D} = (-\frac{3}{2}, \frac{3}{2})^2 \times \mathbb{R}$. As before, there are $I_B = 4$ boundary intersection lines. The evolution of the material surface of the smaller grain is shown at the bottom of Figure 13, where we can see that the square shape quickly rounds to a circle and then shrinks to a point.

We also investigated how the shrinking of the smaller grain in Figure 13 would be affected by different contact angles, if it was also attached to a lower external boundary.

https://doi.org/10.1017/S0956792510000203 Published online by Cambridge University Press

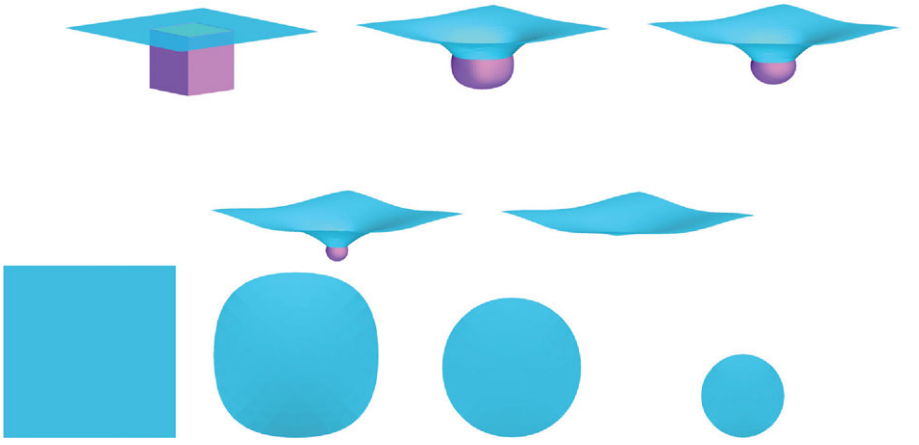

FIGURE 13. (Colour online) Shrinking of a grain. Solution plotted at times $t = 0, 0.025, 0.05, 0.075, 0.1$. Below the surface Γ_1^m at these times.

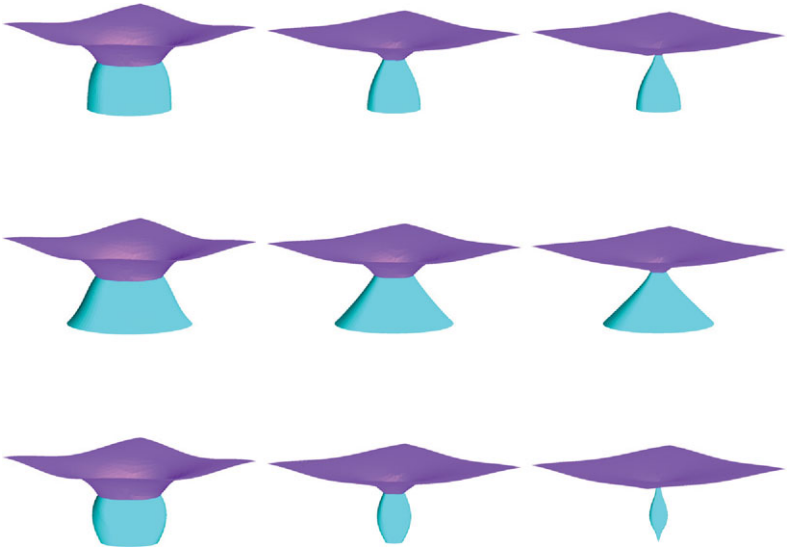

FIGURE 14. (Colour online) Shrinking of a grain attached to a lower boundary with different contact angles. Solution plotted at times $t = 0.05, 0.1, 0.11$ ($\alpha = 90°$), $t = 0.05, 0.1, 0.13$ ($\alpha = 45°$) and $t = 0.05, 0.09, 0.1$ ($\alpha = 120°$).

To this end, we use initial data as in Figure 13, but now choose the external domain to be $\mathscr{D} = (-1, 1)^2 \times (-1, \infty)$ with $I_B = 5$. The discretisation parameters for the simulations are $K = 3553$, $J = 6656$, $\tau = 10^{-3}$, and for the tangential forcing at the lower boundary we choose $\varrho_5 = \cos\alpha$, where $\alpha = 90°$, $45°$ or $120°$, with ϱ_5 denoting the difference in contact energy densities of the external boundary to the outside and to the inside of Γ_3. These contact angles can be easily recognised in Figure 14, where we present the numerical results for these runs.

https://doi.org/10.1017/S0956792510000203 Published online by Cambridge University Press

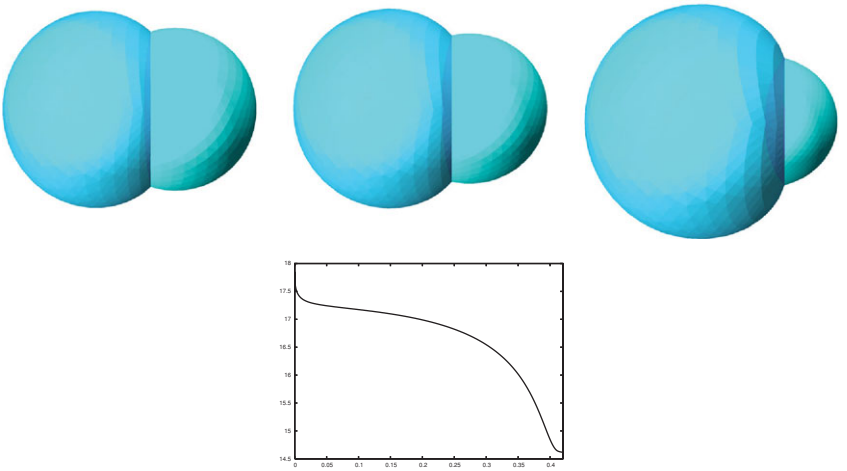

FIGURE 15. (Colour online) Sintering of two particles. Solution plotted at times $t = 0.1$, 0.2, 0.35, with a plot of $E(\Gamma^m)$ below.

Next we present two simulations of sintering, similar to computations performed in [49]. However, we recall that these authors investigated a simplified model, where the fourth-order flows in (2.38) are replaced by volume preserving mean curvature flows, i.e. by second-order flows. In our numerical set-up the material surface is given as the boundary of a double bubble, with the grain boundary separating the two enclosed material volumes. There are no external boundary intersections, and so $I_B = 0$. For the equal volume case, the standard double bubble is a steady state, and no growing or shrinking will occur. However, when the relative volume fraction is not equal to one, the smaller volume will shrink and the larger volume will grow correspondingly, keeping the total material volume constant. In our first numerical experiment, the initial set-up is given as the union of half of a $3:2:2$ ellipsoid and half of a unit ball, so that the relative enclosed volume ratio is $\frac{3}{2}$. The results of a numerical approximation of the shrinking of the smaller volume under the flow (2.38) for $\varsigma = (1, 1, 1)$ is shown in Figure 15, where the discretisation parameters are $K = 3267$, $J = 6240$ and $\tau = 10^{-3}$. In this simulation, the smaller grain disappears at around time $t = 0.42$, and we present a plot of the energy $E(\Gamma^m)$ as defined in (2.9) at the bottom of Figure 15. We repeated the same experiment, but now with the surface energy densities $\varsigma = (\frac{5}{4}, \frac{5}{4}, 1)$, so that $\varsigma_s/\varsigma_{gb} = \frac{5}{4}$ and the dihedral angle (6.2) is 133°, and show the results in Figure 16.

Next we include some experiments that correspond to the simplified two-dimensional model used for the computations in Figure 2, where travelling wave solutions could be observed. Of course, if we start with the exact three-dimensional analogue of Figure 2, then the cluster does not vary in the x_2-direction and the evolution is essentially two-dimensional. In particular, the initial cluster would be given by the flat surfaces $\Gamma_1^0 = [-5,-3] \times [-5,5] \times \{0\}$, $\Gamma_2^0 = [-3,5] \times [-5,5] \times \{0\}$ and $\Gamma_3^0 = [-3,5] \times [-5,5] \times \{-1\} \cup \{-3\} \times [-5,5] \times [-1,0]$; and they all meet the boundary of $\mathscr{D} = (-5,5)^2 \times \mathbb{R}$. In total, there are $I_B = 9$ boundary intersection lines. As the numerical results for this set-up correspond precisely to the two-dimensional simulations shown in Figure 2, we omit these results here.

https://doi.org/10.1017/S0956792510000203 Published online by Cambridge University Press

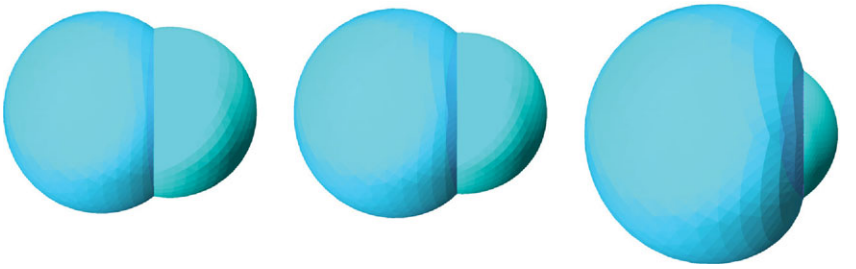

FIGURE 16. (Colour online) Sintering of two particles for $\varsigma = (\frac{5}{4}, \frac{5}{4}, 1)$. Solution plotted at times $t = 0.1, 0.2, 0.35$.

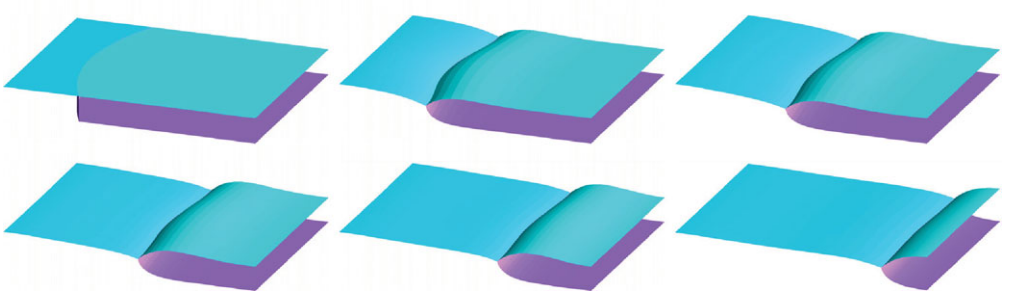

FIGURE 17. (Colour online) Flattening of the triple-junction line profile. Solution plotted at times $t = 0, 0.5, 1, 1.5, 2, 3$.

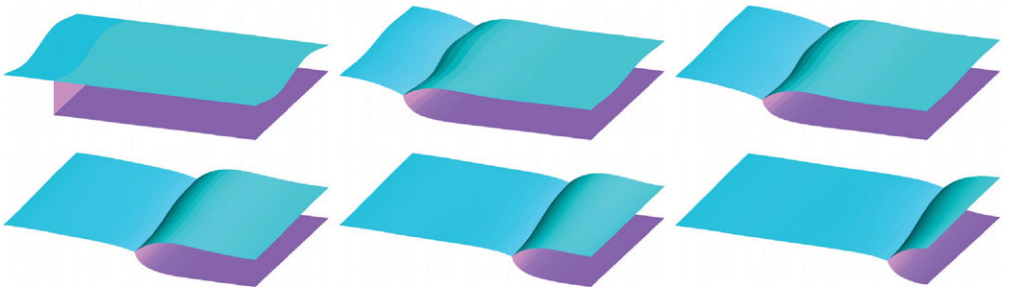

FIGURE 18. (Colour online) Flattening of the triple-junction line profile. Solution plotted at times $t = 0, 0.5, 1, 2, 3, 4$.

Instead, we consider the following truly three-dimensional set-ups. In the first experiment, we used the initial cluster described above, but with an initially curved triple-junction line (see Figure 17). The discretisation parameters for the results shown there are $K = 3479$, $J = 6656$ and $\tau = 10^{-3}$. We observe that the profile of the triple-junction line flattens in time; and it is reasonable to expect that asymptotically the solution will attain the travelling wave profile of the essentially two-dimensional set-up described above.

Similarly, a simulation where the material interface is initialised with a sine profile, which of course is mimicked by the triple-junction line, can be seen in Figure 18. For this run we observe that the height of the triple-junction line becomes uniform in x_2,

https://doi.org/10.1017/S0956792510000203 Published online by Cambridge University Press

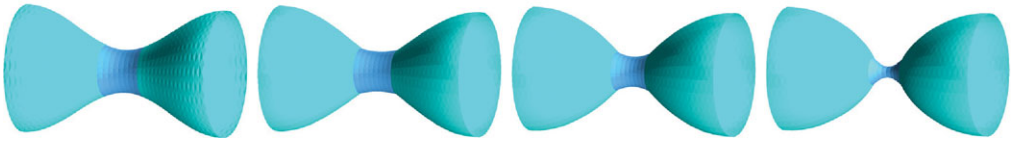

FIGURE 19. (Colour online) Sintering evolution for $\varsigma_s/\varsigma_{gb} = 3$ and $\beta_s = 1$. Plotted at times $t = 0, 0.01, 0.03, 0.05$.

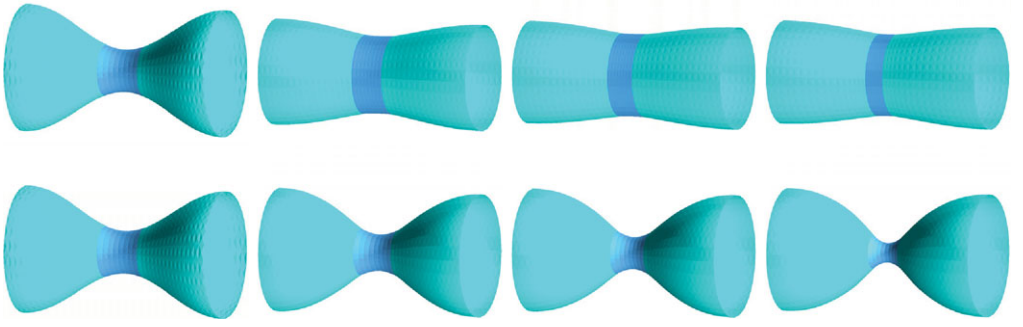

FIGURE 20. (Colour online) Sintering evolution for $\varsigma_s/\varsigma_{gb} = 10$ and $\beta_s = 10$ at times $t = 0, 0.05, 0.6, 1.2$. Below the solution at times $t = 0, 0.01, 0.03, 0.06$ for $\beta_s = 1$.

and that the different heights at time $t = 0$ lead to different speeds of propagation of the triple-junction line in terms of x_2. However, we conjecture that if the simulation was continued in a sufficiently long domain, then the triple-junction line would eventually attain a straight profile, similarly to the evolution shown in Figure 17.

In the next experiment, we consider the three-dimensional analogues of the evolutions shown in Figure 7, i.e. the initial surface cluster is axisymmetric and obtained by rotating the initial configuration in Figure 7 around the x_1-axis. Then the cluster is made up of $I_S = 5$ surfaces which meet at $I_T = 2$ triple-junction lines, with $I_B = 2$ boundary intersection lines; and this models three different grains within a cylindrically shaped material. In our numerical simulations we observed that the behaviour of the solution is distinctively different from the results obtained for the simplified two-dimensional model. In fact, for moderate ratios $\varsigma_s/\varsigma_{gb}$ we observe pinch-off, similar to results reported for the surface diffusion flow of a single hypersurface in [6, Figure 22] (see also [8, Figure 22]). As an example, we show the evolution for $\varsigma_s/\varsigma_{gb} = 3/1 = 3$ and $\beta_s = \beta_{gb} = 1$ in Figure 19, where the discretisation parameters are $K = 2946$, $J = 5632$ and $\tau = 10^{-3}$. Choosing larger mobilities β_s only accelerated the pinching off process, so we omit these results here. However, if we choose a higher ratio $\varsigma_s/\varsigma_{gb} = 10/1 = 10$, and repeated the same experiment for the mobilities $\beta_s = 10$ and $\beta_s = 1$, then we observe a similar behaviour as in Figure 7. In particular, for small mobilities the inner grain vanishes almost immediately, and pinch-off occurs, while for larger mobilities the inner grain grows at first, before it shrinks to a flat disk and vanishes. The computational results are shown in Figure 20. Finally, we recall that the pinch-off observed in Figures 19 and 20 critically depends on the relative length of the cylindrical material slab compared to its largest principal curvature; see e.g. [9] for an analysis in the absence of grain boundaries. In fact, when

https://doi.org/10.1017/S0956792510000203 Published online by Cambridge University Press

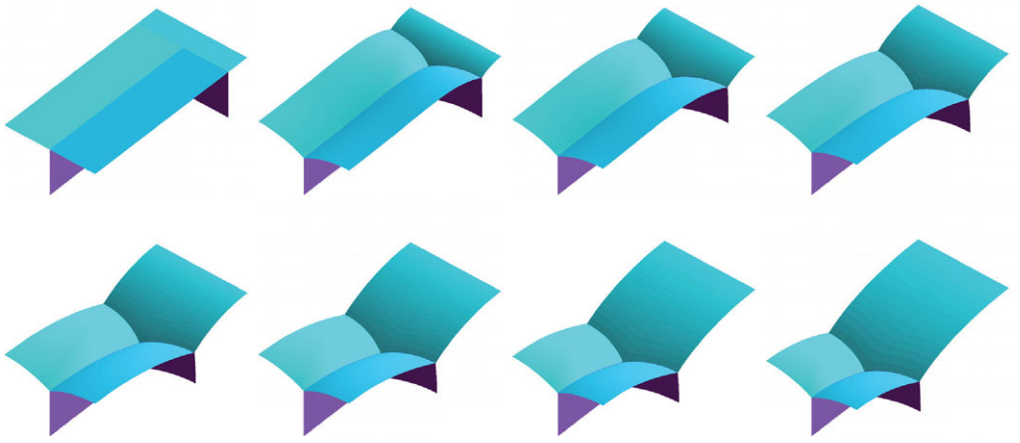

FIGURE 21. (Colour online) Evolution of three grain boundaries in a tricrystal. Plotted at times $t = 0, 0.1, 0.5, 1, 1.5, 2, 2.5, 3$.

we repeated the computations in Figure 19 for a relatively narrower piece of material, no pinch-off was observed and the results are qualitatively similar to the ones at the top of Figure 20, with the middle grain eventually disappearing as it shrinks to a flat disk.

The next experiment is inspired by the AFM image shown in [52, Figure 7], which shows three grain boundaries inside a tricrystal meeting its surface. In particular, on recalling Remark 3.3, we note that here the cluster is given by $I_S = 6$ surfaces meeting at a single quadruple junction point and $I_T = 4$ triple-junction lines, as well as an external boundary along $I_B = 13$ boundary intersection lines. The initially flat surfaces Γ_i^0, $i = 1 \to 6$, all meet the boundary of $\mathscr{D} = (-\frac{7}{2}, \frac{1}{2}) \times (-1, 1) \times (-1, \infty)$. The discretisation parameters are $K = 2822$, $J = 5120$, $\tau = 10^{-3}$ and $T = 3$. In Figure 21 we show the flow under coupled surface and grain boundary motion. We observe a tricrystal analogue of the travelling wave solution for a bicrystal as shown in Figure 2 (see also e.g. Figure 17). In fact, the observed travelling wave solution appears to be a combination of the type of motion in Figure 2 for the material surfaces, as well as the three grain boundaries moving by a natural three-dimensional analogue of the travelling wave solution shown in [2, Figure 15] for the mean curvature flow of a simple curve network, which was studied in e.g. [26, p. 313].

6.2 Anisotropic flows

In what follows we present numerical results similar to the results shown in Section 6.1, but now for fully anisotropic surface energies; i.e. we consider (2.10) with (2.28). Unless otherwise stated, we choose constant mobilities $\beta = (1, 1, 1)$ and set $\gamma = (\gamma_1, \gamma_1, \gamma_1)$, where γ_1 is chosen of the form (2.28).

We start with an experiment as in Figure 17, but now for the anisotropic surface energies $\gamma = (\gamma_s, \gamma_s, |\cdot|)$, where $\gamma_s(\vec{p}) = [25\, p_1^2 + p_2^2 + p_3^2]^{\frac{1}{2}}$. Using the same initial data as in Figure 17, with the discretisation parameters $K = 6857$, $J = 13248$, $\tau = 10^{-3}$ and $T = 3$, we present the evolution for these anisotropies in Figure 22, where we note the

https://doi.org/10.1017/S0956792510000203 Published online by Cambridge University Press

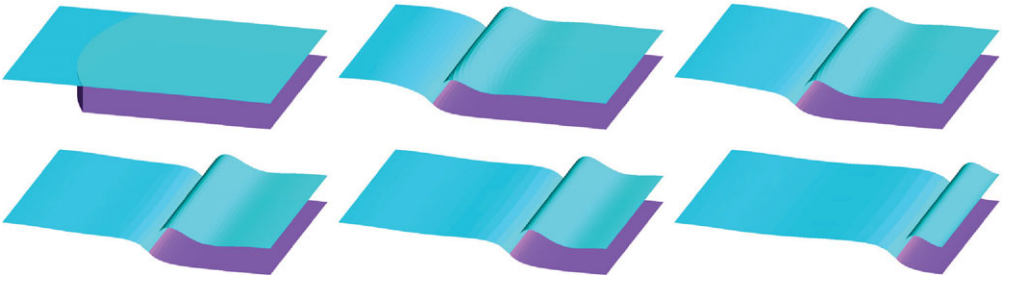

FIGURE 22. (Colour online) Flattening of the triple-junction line profile. Solution plotted at times $t = 0, 0.5, 1, 1.5, 2, 3$.

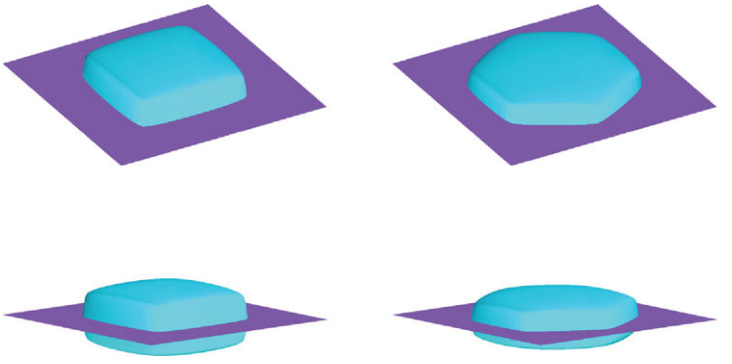

FIGURE 23. (Colour online) Numerical steady states for different anisotropies. The plots show Γ^M from two different points of view.

steep profile of the moving front, similarly to the two-dimensional results in Figure 8. It is also interesting to note, that due to the influence of the chosen anisotropy, the profile of the triple-junction line flattens much quicker compared to the isotropic case presented in Figure 17.

In the next experiment we provide anisotropic versions of the steady states shown in Figure 10. In particular, we choose $\gamma = (\gamma_1, \gamma_1, \gamma_1)$ with $\gamma_1(\vec{p})$ defined as in the first two rows of [7, Figure 1], so that $L = 3$ or $L = 4$. The numerical results, for the same discretisation parameters as in Figure 10, can be seen in Figure 23, where we observe the strong influence of the chosen respective anisotropy.

The sintering of two anisotropic particles is shown in Figure 24. Here we used the anisotropies γ as in Figure 23, and the discretisation parameters and initial surfaces are chosen as in Figure 15. The effect of the different anisotropies is clearly visible during the evolution, as the larger particle grows at the expense of the smaller one.

Finally, we present some anisotropic variants of the simulation in Figure 21, where we recall that these experiments are motivated by the AFM image shown in [52, Figure 7]. Using the same discretisation parameters as in Figure 21, but now starting within the slightly smaller external domain $\mathscr{D} = (-\frac{5}{2}, \frac{1}{2}) \times (-1, 1) \times (-1, \infty)$, we choose the anisotropies $\gamma_i = \varsigma_i \gamma_0$, where γ_0 corresponds to the anisotropy chosen on the right-hand side of Figure 23. Interestingly, we observed very different evolutions for different choices of

https://doi.org/10.1017/S0956792510000203 Published online by Cambridge University Press

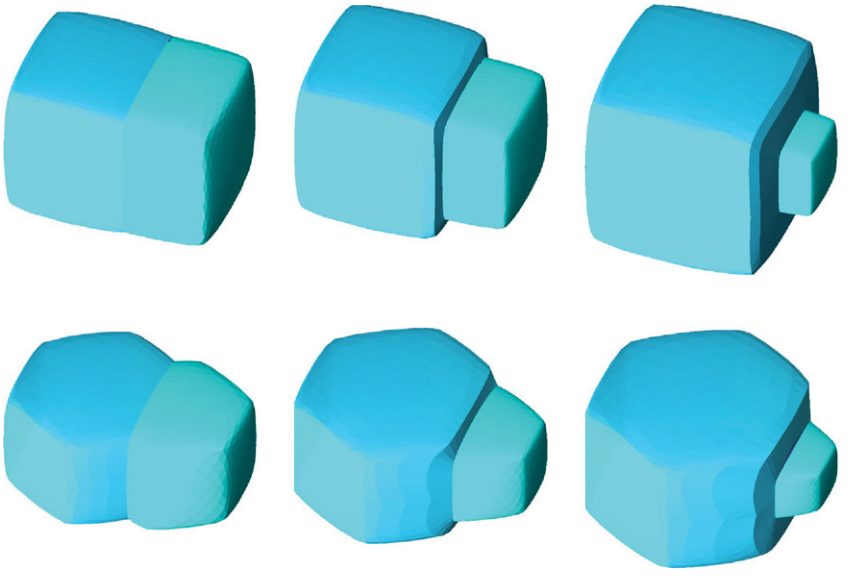

FIGURE 24. (Colour online) Sintering of two anisotropic particles. Solution plotted at times $t = 0.1, 0.7, 0.78$ (above) and $t = 0.1, 0.3, 0.33$ (below).

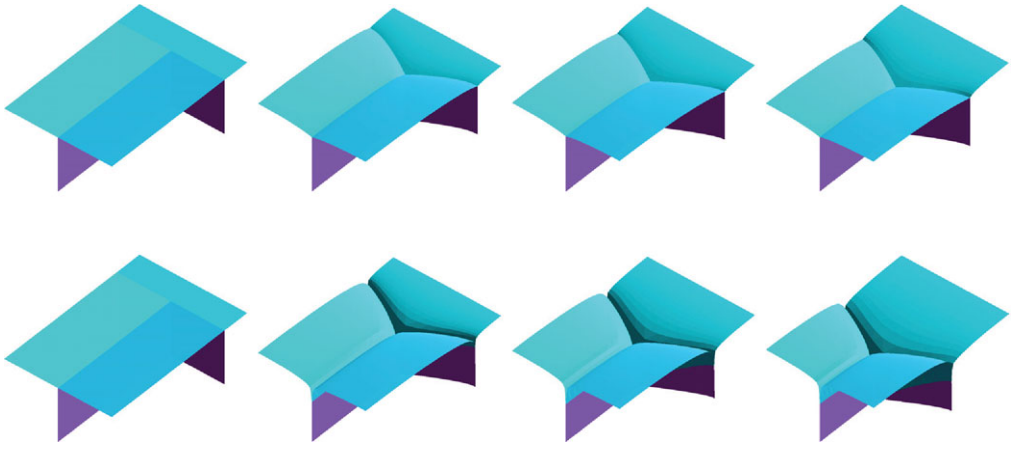

FIGURE 25. (Colour online) Evolution of three grain boundaries in a tricrystal for anisotropic surface energies. Above $\varsigma_s/\varsigma_{gb} = 1/\frac{7}{4} = \frac{4}{7}$, and below for $\varsigma_s/\varsigma_{gb} = 1/2 = \frac{1}{2}$. Plotted at times $t = 0, 0.1, 0.2, 0.3$.

ς_s and ς_{gb}, with a very steep triple-junction line profile for ς_{gb} sufficiently large (see Figure 25).

Conclusions

We presented a variational formulation of coupled surface diffusion and grain boundary motion. These flows have many applications and are used to model physical processes such as thermal grooving and sintering. The mathematical description of such a model

https://doi.org/10.1017/S0956792510000203 Published online by Cambridge University Press

in three-space dimensions involves a surface cluster, where the hypersurfaces making up the cluster undergo either mean curvature flow or surface diffusion. In addition, triple-junction line conditions and conditions at boundary intersection lines have to hold. The generality of our method allows to consider arbitrary types of clusters, with no restriction on the number of surfaces, triple-junction lines, quadruple junction points and boundary intersections.

The introduced variational formulation of the flow, which includes the treatment of non-standard contact angles at the external boundary, leads to a finite-element approximation in a natural way. The presented finite-element approximation, using only conforming piecewise linear elements, can deal with fully anisotropic surface energies and mobilities. The scheme in general is unconditionally stable, straightforward to implement and easy to solve in practice, as the algebraic equations for the discrete unknowns at each time step are linear. Moreover, the resulting triangulations exhibit very good mesh properties, so that no mesh smoothing is required in practice.

Finally, we presented several numerical results in two and three space dimensions, including for anisotropic surface energies. To our knowledge, the three-dimensional simulations are the first such general simulations for three-dimensional coupled surface diffusion and grain boundary motion in the literature. Hence we expect our method to be of great interest to researchers in materials science, engineering, applied mathematics, as well as in geometric measure theory.

References

[1] Barbosa, J. L., do Carmo, M. & Eschenburg, J. (1988) Stability of hypersurfaces of constant mean curvature in Riemannian manifolds. *Math. Z.* **197**, 123–138.

[2] Barrett, J. W., Garcke, H. & Nürnberg, R. (2007a) On the variational approximation of combined second and fourth order geometric evolution equations. *SIAM J. Sci. Comput.* **29**, 1006–1041.

[3] Barrett, J. W., Garcke, H. & Nürnberg, R. (2007b) A phase field model for the electromigration of intergranular voids. *Interfaces Free Bound.* **9**, 171–210.

[4] Barrett, J. W., Garcke, H. & Nürnberg, R. (2008a) Numerical approximation of anisotropic geometric evolution equations in the plane. *IMA J. Numer. Anal.* **28**, 292–330.

[5] Barrett, J. W., Garcke, H. & Nürnberg, R. (2008b) On sharp interface limits of Allen–Cahn/Cahn–Hilliard variational inequalities. *Discrete Contin. Dyn. Syst. Ser.* S **1**, 1–14.

[6] Barrett, J. W., Garcke, H. & Nürnberg, R. (2008c) On the parametric finite element approximation of evolving hypersurfaces in $\mathbb{R}^3$. *J. Comput. Phys.* **227**, 4281–4307.

[7] Barrett, J. W., Garcke, H. & Nürnberg, R. (2008d) A variational formulation of anisotropic geometric evolution equations in higher dimensions. *Numer. Math.* **109**, 1–44.

[8] Barrett, J. W., Garcke, H. & Nürnberg, R. (2010) Parametric approximation of surface clusters driven by isotropic and anisotropic surface energies. *Interfaces Free Bound.* **12**, 187–234.

[9] Bernoff, A. J., Bertozzi, A. L. & Witelski, T. P. (1998) Axisymmetric surface diffusion: Dynamics and stability of self-similar pinchoff. *J. Stat. Phys.* **93**, 725–776.

[10] Blackford, J. R. (2007) Sintering and microstructure of ice: A review. *J. Phys.* D: Appl. Phys. **40**, 355–384.

[11] Brakke, K. A. (1992) The surface evolver. *Exp. Math.* **1**, 141–165.

https://doi.org/10.1017/S0956792510000203 Published online by Cambridge University Press

[12] Bronsard, L., Garcke, H. & Stoth, B. (1998) A multi-phase Mullins–Sekerka system: Matched asymptotic expansions and an implicit time discretisation for the geometric evolution problem. *Proc. R. Soc. Edinburgh Sect.* A **128**, 481–506.
[13] Cahn, J. W. & Hoffman, D. W. (1974) A vector thermodynamics for anisotropic surfaces. II. Curved and faceted surfaces. *Acta Metall.* **22**, 1205–1214.
[14] Ch'ng, H. N. & Pan, J. (2004) Cubic spline elements for modelling microstructural evolution of materials controlled by solid-state diffusion and grain-boundary migration. *J. Comput. Phys.* **196**, 724–750.
[15] Ch'ng, H. N. & Pan, J. (2005) Modelling microstructural evolution of porous polycrystalline materials and a numerical study of anisotropic sintering. *J. Comput. Phys.* **204**, 430–461.
[16] Ch'ng, H. N. & Pan, J. (2007) Sintering of particles of different sizes. *Acta Mater.* **55**, 813–824.
[17] Concus, P. & Finn, R. (1974) On capillary free surfaces in the absence of gravity. *Acta Math.* **132**, 177–198.
[18] Davi, F. & Gurtin, M. E. (1990) On the motion of a phase interface by surface diffusion. *Z. Angew. Math. Phys.* **41**, 782–811.
[19] Deckelnick, K., Dziuk, G. & Elliott, C. M. (2003) Error analysis of a semidiscrete numerical scheme for diffusion in axially symmetric surfaces. *SIAM J. Numer. Anal.* **41**, 2161–2179.
[20] Dziuk, G. (1988) Finite elements for the Beltrami operator on arbitrary surfaces. In: S. Hildebrandt & R. Leis (editors), *Partial Differential Equations and Calculus of Variations*, Vol. 1357, Lecture Notes in Mathematics, Springer-Verlag, Berlin, pp. 142–155.
[21] Dziuk, G. (1991) An algorithm for evolutionary surfaces. *Numer. Math.* **58**, 603–611.
[22] Dziuk, G. (1994) Convergence of a semi-discrete scheme for the curve shortening flow. *Math. Models Methods Appl. Sci.* **4**, 589–606.
[23] Dziuk, G. & Elliott, C. M. (2007) Surface finite elements for parabolic equations. *J. Comput. Math.* **25**, 385–407.
[24] Finn, R. (1986) Equilibrium capillary surfaces. *Grundlehren der Mathematischen Wissenschaften*, Vol. 284, Springer-Verlag, New York.
[25] Garcke, H., Nestler, B. & Stoth, B. (1998) On anisotropic order parameter models for multi-phase systems and their sharp interface limits. *Physica* D **115**, 87–108.
[26] Garcke, H., Nestler, B. & Stoth, B. (1999) A multiphase field concept: Numerical simulations of moving phase boundaries and multiple junctions. *SIAM J. Appl. Math.* **60**, 295–315.
[27] Garcke, H. & Novick-Cohen, A. (2000) A singular limit for a system of degenerate Cahn–Hilliard equations. *Adv. Differ. Equ.* **5**, 401–434.
[28] Garcke, H. & Wieland, S. (2006) Surfactant spreading on thin viscous films: Nonnegative solutions of a coupled degenerate system. *SIAM J. Math. Anal.* **37**, 2025–2048.
[29] Hestenes, M. R. (1975) Pseudoinverses and conjugate gradients. *Commun. ACM* **18**, 40–43.
[30] Hildebrandt, S. & Tromba, A. (1996) *The Parsimonious Universe. Shape and Form in the Natural World*, Copernicus, New York.
[31] Kanel, J., Novick-Cohen, A. & Vilenkin, A. (2003) A traveling wave solution for coupled surface and grain boundary motion. *Acta Mater.* **51**, 1981–1989.
[32] Kanel, J., Novick-Cohen, A. & Vilenkin, A. (2004) Coupled surface and grain boundary motion: Nonclassical traveling wave solutions. *Adv. Differ. Equ.* **9**, 299–327.
[33] Kanel, J., Novick-Cohen, A. & Vilenkin, A. (2005) A numerical study of grain boundary motion in bicrystals. *Acta Mater.* **53**, 227–235.
[34] Kanel, J., Novick-Cohen, A. & Vilenkin, A. (2006) Numerical analysis of a 3d radially symmetric shrinking grain attached to a free crystal surface. *Acta Mater.* **54**, 2589–2595.
[35] Kucherenko, S., Pan, J. & Yeomans, J. A. (2000) A combined finite element and finite difference scheme for computer simulation of microstructure evolution and its application to pore-boundary separation during sintering. *Comput. Mater. Sci.* **18**, 76–92.
[36] Moelans, N., Blanpain, B. & Wollants, P. (2007) A phase field model for grain growth and thermal grooving in thin films with orientation dependent surface energy. *Solid State Phenomena* **129**, 89–94.

[37] Mullins, W. W. (1958) The effect of thermal grooving on grain boundary motion. *Acta Metall.* **6**, 414–427.
[38] Novick-Cohen, A. (2000) Triple-junction motion for an Allen–Cahn/Cahn–Hilliard system. *Physica* D **137**, 1–24.
[39] Pan, J. (2003) Modelling sintering at different length scales. *Int. Mater. Rev.* **48**, 69–85.
[40] Pan, J. & Cocks, A. C. F. (1995) A numerical technique for the analysis of coupled surface and grain-boundary diffusion. *Acta Mater.* **43**, 1395–1406.
[41] Pan, J., Cocks, A. C. F. & Kucherenko, S. (1997) Finite element formulation of coupled grain-boundary and surface diffusion with grain-boundary migration. *Proc. R. Soc. Lond. Ser.* A **453**, 2161–2184.
[42] Pan, Z. & Wetton, B. (2008) A numerical method for coupled surface and grain boundary motion. *Eur. J. Appl. Math.* **19**, 311–327.
[43] Schmidt, A. & Siebert, K. G. (2005) *Design of Adaptive Finite Element Software: The Finite Element Toolbox ALBERTA*, Vol. 42, Lecture Notes in Computational Science and Engineering, Springer-Verlag, Berlin.
[44] Sun, B. & Suo, Z. (1997) A finite element method for simulating interface motion. II. Large shape change due to surface diffusion. *Acta Mater.* **45**, 4953–4962.
[45] Sun, B., Suo, Z. & Yang, W. (1997) A finite element method for simulating interface motion. I. Migration of phase and grain boundaries. *Acta Mater.* **45**, 1907–1915.
[46] Taylor, J. E. & Cahn, J. W. (1994) Linking anisotropic sharp and diffuse surface motion laws via gradient flows. *J. Stat. Phys.* **77**, 183–197.
[47] Tritscher, P. (1999) Thermal grooving by surface diffusion for an extended bicrystal abutting a half-space. *R. Soc. Lond. Proc. Ser.* A Math. Phys. Eng. Sci. **455**, 1957–1977.
[48] Vilenkin, A. J., Kris, R. & Brokman, A. (1997) Breakup and grain growth in thin-film array. *J. Appl. Phys.* **81**, 238–245.
[49] Wakai, F., Yoshida, M., Shinoda, Y. & Akatsu, T. (2005) Coarsening and grain growth in sintering of two particles of different sizes. *Acta Mater.* **53**, 1361–1371.
[50] Zhang, H. & Wong, H. (2002a) Coupled grooving and migration of grain boundaries: Regime I. *Acta Mater.* **50**, 1983–1994.
[51] Zhang, H. & Wong, H. (2002b) Coupled grooving and migration of grain boundaries: Regime II. *Acta Mater.* **50** (2002), 1995–2012.
[52] Zhang, W. & Gladwell, I. (2005) Thermal grain boundary grooving with anisotropic surface free energy in three dimensions. *J. Cryst. Growth* **277** , 608–622.